

The ELM Survey South. II. Two dozen new low mass white dwarf binaries.

ALEKZANDER KOSAKOWSKI ,¹ WARREN R. BROWN ,² MUKREMIN KILIC ,³ THOMAS KUPFER ,¹
 ANTOINE BÉDARD ,⁴ A. GIANNINAS ,⁵ MARCEL A. AGÜEROS ,^{6,7} AND MANUEL BARRIENTOS ,³

¹Department of Physics and Astronomy Texas Tech University 2500 Broadway Lubbock, Texas 79409, USA

²Center for Astrophysics, Smithsonian Astrophysical Observatory 60 Garden St., Cambridge, MA, 012138 USA

³Homer L. Dodge Department of Physics and Astronomy University of Oklahoma 1667 K Street NW, Suite 800 Norman, OK 73072, USA

⁴Department of Physics, University of Warwick, Gibbet Hill Road, Coventry CV4 7AL, United Kingdom

⁵Physics Department, Trinity College 330 Summit Street Hartford, CT 06106, USA

⁶Department of Astronomy, Columbia University, 550 West 120th Street, New York, NY 10027, USA

⁷Laboratoire d'astrophysique de Bordeaux, Univ. Bordeaux, CNRS, B18N, Allée Geoffroy Saint-Hilaire, 33615 Pessac, France

ABSTRACT

We present the results from our ongoing spectroscopic survey targeting low mass white dwarf binaries, focusing on the southern sky. We used a Gaia DR2 and eDR3 based selection and identified 28 new binaries, including 19 new extremely low mass white dwarfs, one short period, likely eclipsing, DABZ, and two potential LISA binaries. We present orbital and atmospheric parameters for each new binary based on our spectroscopic follow-up.

Four of our new binaries show periodic photometric variability in the TESS 2-minute cadence data, including one new eclipsing double-lined spectroscopic binary. Three others show periodic photometric variability in ZTF, including one new eclipsing binary. We provide estimates for the inclinations and scaled component radii for these ZTF variables, based on light curve modeling to our high-speed photometric follow-up observations.

Our observations have increased the sample of ELM Survey binaries identified in the southern sky to 41, an increase of 64%. Future time domain surveys, such as BlackGEM and the Vera C. Rubin Observatory Legacy Survey of Space and Time, will efficiently identify the photometric variables in the southern sky and significantly increase the population of southern sky low mass white dwarf binaries, leading to a more complete all-sky population of these systems.

Keywords: Compact Binaries — Eclipsing Binary — White Dwarfs — Spectroscopy

1. INTRODUCTION

Extremely Low Mass (ELM; $M \lesssim 0.3 M_{\odot}$) white dwarfs are a relatively rare class of He-core white dwarfs which form after early severe mass loss. Because the main sequence lifetime of low mass stars can exceed a Hubble time, the ELM white dwarfs observed today are not expected to have formed through single star evolution. With an exception for the extreme mass loss of high-metallicity stars (see Kilic et al. 2007), ELM white dwarfs are expected to form through binary evolution, including one or more episodes of common envelope evolution (Li et al. 2019). The result of this binary evolution is a population of evolved compact binaries containing low mass He-core white dwarfs with evolved companions.

These low mass white dwarf binaries are important for studying both binary evolution and formation rates of various exotic systems. Shen (2015) and Brown et al. (2016b) show that most white dwarf binaries may merge and form other exotic systems such as extreme Helium stars (Zhang et al. 2014), accreting AM CVn binaries (Kilic et al. 2016), or massive single white dwarfs (Kilic et al. 2023). Binaries with well-constrained physical parameters have also been used to place constraints on the efficiency of common envelope ejection (see Scherbak & Fuller 2023).

The ELM Survey (Brown et al. 2010; Kilic et al. 2011; Brown et al. 2012; Kilic et al. 2012; Brown et al. 2013; Gianninas et al. 2015; Brown et al. 2016a, 2020, 2022) is a spectroscopic survey targeting these low-mass white

dwarf binaries based on photometry from sky surveys, such as SDSS (Abazajian et al. 2003) and PanSTARRs (Chambers et al. 2016). Kosakowski et al. (2020) expanded the ELM Survey into the southern sky using photometry from SkyMapper (Onken et al. 2019) and VST ATLAS (Shanks et al. 2015), and found that a Gaia based selection is efficient for identifying ELM white dwarf binaries. In total, previous ELM Survey studies have constrained the orbits and atmospheric parameters of 120 unique low mass white dwarf binaries (Brown et al. 2020; Kosakowski et al. 2020; Brown et al. 2022). Similar studies have created catalogs of ELM white dwarf candidates using Gaia DR2 astrometry (see Pelisoli & Vos 2019) and single-epoch spectroscopy from LAMOST DR8 (see Wang et al. 2022), many of which still require follow-up observations to confirm their nature.

In this work, we continue the ELM Survey South with our search for low mass white dwarf binaries in the southern sky using a Gaia DR2 and eDR3. While we focused on objects in the southern sky, our Gaia based selection included many Northern sky objects, which we include in this work.

2. TARGET SELECTION

Our target selection made use of parallax and color measurements from Gaia DR2 and eDR3, based on previous ELM Survey discoveries. Figure 1 displays the locations of our observed objects on the Gaia DR3 color-magnitude diagram. The 28 new binaries from this work are plotted with blue symbols while previous ELM Survey binaries are plotted as black symbols. Green points represent other objects observed as part of this work with PARALLAX_OVER_ERROR >3 , PARALLAX >0.5 , and no cuts to RUWE, for which we have obtained at least one optical spectrum. We draw a box around the region surrounding the main concentration of ELM Survey ELM white dwarf binaries, defined by

$$\begin{aligned} -0.24 < (BP - RP) < 0.34, \\ M_G > 4.31(BP - RP) + 5.53, \\ M_G < 4.31(BP - RP) + 10.53. \end{aligned}$$

Within this box, we have observed 217 objects, including the 28 new LMWD binaries presented in this work. Among our observed objects, we identify 27 additional ELM white dwarf candidates based on model atmosphere fits to our follow-up spectroscopy, including 17 which fall within the parameter space of the “clean” sample of ELM white dwarfs of Brown et al. (2020). Our ongoing follow-up finds that at least half of these spectroscopic candidates show significant radial velocity variability, but have unconstrained orbital parameters.

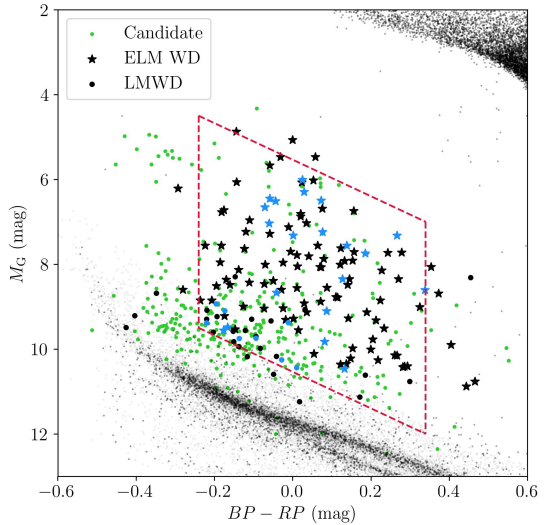


Figure 1. Gaia color-magnitude diagram showing the target selection box described in the text. The 28 new binaries identified in this work are represented with blue symbols, while the previous ELM Survey binaries are represented as black symbols. Stars represent ELM white dwarfs ($M \lesssim 0.3 M_{\odot}$). Filled-circles represent low mass white dwarfs. Green circles represent our observed candidates selected through our Gaia DR2 and eDR3 selection.

These additional binaries will be presented in a future publication. Most of our observed sample contains single white dwarfs with $\log g \approx 7.5$.

3. OBSERVATIONS

We used a similar observing strategy as in previous ELM Survey publications: We obtained one optical spectrum for each of our candidates to confirm their nature and perform spectroscopic fitting with model atmospheres. For objects consistent with ELM white dwarfs ($5.0 \lesssim \log g \lesssim 7.2$), we obtained multiple additional spectra to check for radial velocity variability and constrain orbital periods. Candidates which do not show significant radial velocity variability, or which show atmospheric parameters inconsistent with ELM white dwarfs, are excluded from extensive follow-up.

Our observing strategy favors identifying short period binaries ($P \lesssim 6$ h) with large velocity semi-amplitudes, which form through common envelope interaction. Binaries with longer orbital periods and lower velocity semi-amplitudes, which likely form through stable Roche Lobe overflow, are less likely to be detected and constrained through our observing strategy, while those that are identified require more resources to constrain through radial velocity follow-up.

In this section we briefly describe the resources used for our follow-up observations, including the telescopes, instruments, and configurations.

3.1. Southern Astrophysical Research Telescope (SOAR)

We used the SOAR 4.1-meter telescope with the Goodman spectrograph (Clemens et al. 2004) configured with the 930 lines mm⁻¹ grating and 1.01'' slit, resulting in a spectral resolution ≈ 2.6 Å over the wavelength range 3550 – 5300 Å. These data were taken as part of the NOAO programs 2019B-0004, 2020B-0013, and 2021A-0007, and NOIRLab 2022A-161017.

3.2. Gemini South

We used the Gemini South 8.1-meter telescope, located on Cerro Pachón in Chilé, with the GMOS-S spectrograph configured with the 0.5'' and 1.0'' slits and the B600 grating (600 lines mm⁻¹) in first-order centered on $\lambda_{center} = 5150$ Å. These configurations resulted in resolutions ≈ 2.8 Å and ≈ 5.5 Å over the spectral range 3600 – 6750 Å, respectively. These data were obtained as part of the programs GN-2021A-Q-300, GS-2020B-Q-304, GS-2021A-Q-300, GS-2021B-Q-304.

3.3. Walter-Baade Magellan Telescope

We used the 6.5-meter Walter-Baade Magellan 1 Telescope at the Las Campanas Observatory in Chilé with the Magellan Echellette (MagE) spectrograph and the 0.85'' slit, resulting in a resolving power $R \approx 4800$ covering the wavelength range 3600 – 7000 Å.

3.4. Fred Lawrence Whipple Observatory (FLWO)

We used the 1.5-meter Tillinghast telescope at FLWO located on Mt. Hopkins in Arizona. Our primary setup used FAST spectrograph with the 1.5'' slit and 300 lines mm⁻¹ grating, resulting in spectral resolution ≈ 3.6 Å covering the spectral range 3500 – 7400 Å. A handful of observations used a slightly different setup with the 1.5 Å slit and 600 lines mm⁻¹ grating, resulting in spectral resolution ≈ 1.8 Å covering the spectral range 3650 – 5300 Å.

3.5. MMT Observatory

We used the 6.5-meter MMT with the blue channel spectrograph, primarily with the 1.25'' slit and 832 lines mm⁻¹ grating, resulting in ≈ 1.2 Å resolution over the wavelength range 3600 – 4500 Å. However, a handful of our observations used the 1.0'' slit with the 832 lines mm⁻¹ grating, resulting in spectral resolution ≈ 1.0 Å over roughly same wavelength range.

3.6. MDM Observatory

We used the 2.4-meter Hiltner telescope at the MDM observatory, located in Kitt Peak, Arizona, with the OS-MOS spectrograph, the 1.2'' slit, and the blue grism ($R \sim 1600$), resulting in spectral resolution 3.6 Å over the wavelength range 3600 – 5930 Å.

3.7. McDonald Observatory

We used the 2.1-meter Otto Struve telescope at the McDonald Observatory near Fort Davis, Texas to obtain high-speed photometric follow-up of our binaries to confirm variability seen in various sky survey data archives. We used the ProEM frame-transfer CCD detector with either the BG40, g -, r -, or i -band filters.

4. SPECTROSCOPIC ANALYSIS

4.1. Data Reduction and Calibration

Data reduction was performed using standard IRAF procedures, including bias correction, flat-fielding, aperture extraction, wavelength calibration, and flux calibration with spectro-photometric standard star observations obtained on the same night as each science exposure.

To ensure an accurate wavelength solution for each spectrum, we paired each science exposure with a calibration lamp spectrum taken within ≈ 15 min at the same telescope position as the corresponding science exposure, resulting in wavelength calibration accuracy of 2 – 3 km s⁻¹, as tested against night sky lines.

4.2. Radial Velocities

We measured the radial velocity of each of our spectra using a cross-correlation method with the IRAF package XCSAO (Kurtz & Mink 1998). Each spectrum was cross-correlated with a low-mass white dwarf template spectrum and corrected to zero-velocity. We combined the individual zero-velocity object-specific spectra to create a single high-quality, zero-velocity, spectrum for each object which we use for atmospheric modeling. Finally, we cross-correlated the combined zero-velocity template spectrum for each object with their single-exposure component spectra to obtain our final radial velocity measurements. Our radial velocity measurements for each binary are presented in Table 4. We fit a circular orbit to our radial velocity measurements using a Monte Carlo approach based on Kenyon & Garcia (1986) to estimate orbital period P , velocity semi-amplitude K , and systemic velocity γ .

4.3. Atmospheric Parameters

We estimated the atmospheric parameters T_{eff} and $\log g$ for the primary star in each of our binaries through

fitting a grid of 1-D pure-hydrogen atmosphere models to our high signal-to-noise, combined, zero-velocity spectra. The details of this process are described in Gianninas et al. (2011, 2014, 2015). In short: we applied a Levenberg-Marquardt minimization algorithm to fit the normalized Balmer line profiles of H β through H12, where visible, to a grid of pure-hydrogen model atmospheres convolved to the spectral resolution of the observed spectra, defined by the observation instrument setup. Our parameter estimates are reliable for binaries in which the companion does not contribute a significant amount to the total system light.

Cool objects, with temperatures $T_{\text{eff}} \lesssim 10,000$ K return systematically large $\log g$ when fit with 1D stellar models (see Tremblay et al. 2011). Thus, we apply a 3D correction to the fits of cool objects using the equations provided in Tremblay et al. (2015).

Our minimization process returns internal uncertainties which are most sensitive to the flux calibration and signal-to-noise ratio of the input spectrum. We add in quadrature the external uncertainties of $\sigma_{T_{\text{eff}}} = 1.4\%$ and $\sigma_{\log g} = 0.042$ dex, as presented in Liebert et al. (2005), to each of our reported values.

Table 5 presents the atmospheric parameters for our observed sample (Figure 1: green points) with $\log g > 5.0$. A representative optical spectrum for many of these objects is available in an online Zenodo archive¹ (Kosakowski et al. 2023) in FITS format.

5. ARCHIVAL LIGHT CURVE DATA

Large scale time domain surveys are a valuable resource for efficiently identifying transients and periodic variables. While these time domain surveys do not replace conventional target selection methods, when paired with color surveys and the precise astrometry from Gaia, it is possible to efficiently perform follow-up observations for characterizing photometrically variable sources.

We made use of the publicly-available online data archives of the Transiting Exoplanet Survey Satellite (TESS; Ricker et al. 2015) and the Zwicky Transient Facility (ZTF; Bellm et al. 2019; Graham et al. 2019; Masci et al. 2019) DR10 to confirm photometric variability in our targets and constrain orbital periods.

We used the computational resources of the Texas Tech University High Performance Computing Center to perform searches for periodic variability in each of our target light curves from both the TESS and ZTF

public data archives. We used two algorithms to identify different types of photometric variability:

For sinusoidal variability, typically caused by a tidally-distorted star in a compact binary, relativistic beaming, strong reflection effects, stellar rotation, or low-amplitude pulsations, we used the ASTROPY (Astropy Collaboration et al. 2013, 2018, 2022) implementation of the Lomb-Scargle (LS) periodogram (Lomb 1976; Scargle 1982; VanderPlas 2018), searching periods between 5 min and 684 min.

To identify eclipsing binaries, we make use of a generic Box Least Squares (BLS; Kovács et al. 2002) algorithm, which attempts to fit box-shaped eclipses to light curve data phase-folded at periods within the provided frequency grid. Specifically, our BLS algorithm searched for eclipse duration between 0.1% and 10.0% of the orbit and orbital periods between 5 min and 684 min. The BLS algorithm is ideal for identifying eclipsing systems with sharp ingress and egress features, such as eclipsing binaries containing white dwarfs.

5.1. TESS High Cadence Data Archive

TESS is a space-based all-sky survey satellite designed to identify exoplanets through transit detections in 27-day long pointings, covering a 24×96 deg² field of view in a broadband filter ($\approx 6000 - 10,000$ Å). The original mission (2018-2020) obtained 30-minute cadence data in Full Frame Images (FFI) with select fields obtaining 2-minute high-cadence observations. The recent extended mission (2020-2022) has improved these to 10-minute cadence FFIs and 20-second high-cadence fields. While the plate scale for TESS is large ($\approx 21'' \text{ px}^{-1}$), objects that show photometric variability in TESS data are typically very well-sampled.

We searched the Barbara A. Mikulski Archive for Space Telescopes (MAST), through the Python module ASTROQUERY.MAST², to identify the TESS Input Catalog (TIC; Stassun et al. 2018) target ID for each of our objects. Using the TIC ID, we downloaded the TESS 2-minute and 20-second cadence light curve data through the online TESS archive³.

For each sector of TESS data we recovered, we removed lower quality data, based on bit flags described on the TESS Data Quality Overview webpage⁴, following the steps outlined in the Jupyter Notebook examples provided through the Space Telescope Science Institute's

² <https://astroquery.readthedocs.io/en/latest/mast/mast.html>

³ https://archive.stsci.edu/tess/bulk_downloads/bulk_downloads_fits_lc-dv.html

⁴ <https://outerspace.stsci.edu/display/TESS/2.0+-+Data+Product+Overview>

¹ <https://doi.org/10.5281/zenodo.7849976>

GitHub page⁵. We combined data across multiple sectors by simply dividing each sector’s light curve by its median PDCSAP flux value (aperture photometry corrected for common instrumental systematics and trends) and appending each scaled sector light curve together.

5.2. ZTF Data Archive

ZTF is an optical time-domain survey designed to image the entire Northern sky down to ≈ 20.5 mag every two days in two filters, ZTF-*g* and ZTF-*r*, with ZTF-*i* sampled less frequently. The ZTF survey uses the 48-inch Schmidt Telescope at the Palomar Observatory in California with a 48 deg² field of view.

We performed a cone-search on the public Data Release⁶ 10 (DR10) data archive using a 5'' search radius centered on the Gaia DR2 or eDR3 coordinates for each of our objects. Because ZTF assigns different object IDs for the same object in different filters, we combined data for object detections within 2.5'' of each coordinate pair returned within our 5'' search radius. This process separates nearby ($2.5'' < d < 5.0''$) objects in relatively crowded fields.

To increase the temporal sampling of the ZTF light curves, we artificially shifted the *r*-band and *i*-band data such that their median magnitudes matched the median value of the *g*-band data. We then used this median-combined light curve in our periodicity search.

Many of our objects which show short-period photometric variability in ZTF were included in the ZTF deep-drilling survey, which targets specific fields for continuous observations over ≈ 90 min in the ZTF-*r* band (Kupfer et al. 2021). These deep drilling fields provide significant orbital phase coverage that would otherwise be relatively sparse in the standard ZTF northern sky survey.

6. RESULTS

We have constrained the atmospheric parameters and orbital periods for 28 new binaries identified through our target selections. In this section, we present details for the eight binaries which require additional explanation, such as those with additional constraints from light curve data or those with unusual spectra. The remaining objects are summarized in Table 1. We display the log g - T_{eff} distribution for each of these objects in Figure 2.

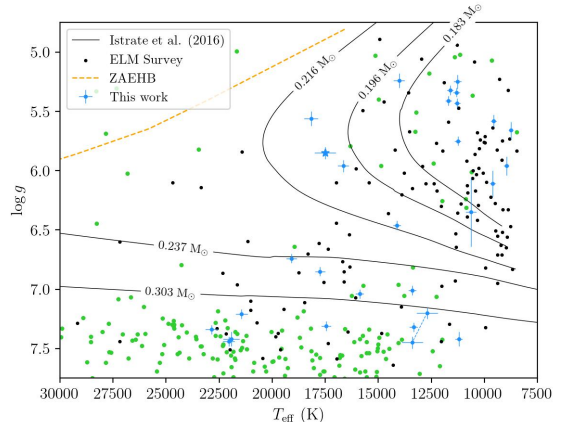


Figure 2. $\log g$ - T_{eff} distribution of low mass white dwarfs identified as part of the ongoing ELM Survey. Previous ELM Survey binaries are displayed as black points. New binaries from this work are colored blue. Other objects observed as part of this work are colored green. We overplot the cooling tracks for $0.183 M_{\odot}$, $0.196 M_{\odot}$, $0.216 M_{\odot}$, $0.237 M_{\odot}$, and $0.303 M_{\odot}$ white dwarfs with $Z = 0.001$ from Istrate et al. (2016), including rotation and diffusion. We mark the location of the DABZ J2049+3351 with a blue star symbol and use a dashed line to connect the markers for the individual stars in the double-lined binary J2102-4145. The Zero-Age Extreme Horizontal Branch (ZAEHB) is colored as an orange dashed line for reference.

J0215+0155

We obtained 112 radial velocity measurements for J021506.244+015503.363 (J0215+0155; GAIA DR3 2513538251735261696), resulting in best-fitting orbital parameters $P_{\text{RV}} = 9.3106$ h, $K = 186.4 \pm 1.5$ km s⁻¹, and $\gamma = -49.4 \pm 1.1$ km s⁻¹. Together with Gaia DR3 astrometry, we estimated the Galactic space velocities $[U, V, W] = [121 \pm 1, -37 \pm 1, -59 \pm 1]$ km s⁻¹, (U positive towards the Galactic center), corrected for the motion of the local standard of rest (Schönrich et al. 2010).

We determine Galactic disk and halo membership by computing the Mahalanobis distance between the measured Galactic space velocities and the velocity distributions for thick disk and halo populations using average velocities and velocity dispersions from (Chiba & Beers 2000). Specifically, we compared against velocity distributions defined by $[\langle U \rangle, \langle V \rangle, \langle W \rangle]_{\text{Disk}} = [4 \pm 46, -20 \pm 50, -3 \pm 35]$ km s⁻¹ and $[\langle U \rangle, \langle V \rangle, \langle W \rangle]_{\text{Halo}} = [17 \pm 141, -187 \pm 106, -5 \pm 94]$ km s⁻¹ for the thick disk and halo, respectively. Our measurements for J0215+0155 are consistent with Galactic halo membership.

Our pure-hydrogen model atmosphere fits to the summed zero-velocity spectrum of J0215+0155 result in best-fitting atmospheric parameters $T_{\text{eff}} = 11,310 \pm$

⁵ <https://github.com/spacetelescope/notebooks/>

⁶ <https://www.ztf.caltech.edu/ztf-public-releases.html>

Object Name	R.A. (2016.0)	Decl. (2016.0)	T_{eff} (K)	$\log g$ (cm s $^{-2}$)	M_1 (M_{\odot})	Gaia G (mag)	Gaia Parallax (mas)
J0135+2359	01:35:00.856	+23:59:46.091	14130 ± 210	6.46 ± 0.05	0.21 ± 0.04	18.7	1.18 ± 0.29
J0155–4148	01:55:34.866	–41:48:18.433	11250 ± 170	5.75 ± 0.05	0.22 ± 0.02	15.7	2.08 ± 0.03
J0215+0155 ^{a,c}	02:15:06.244	+01:55:03.363	11310 ± 180	5.34 ± 0.05	0.29 ± 0.02	14.3	2.15 ± 0.03
J0221+1710 ^{b,c}	02:21:10.832	+17:10:49.182	13400 ± 200	7.01 ± 0.04	0.27 ± 0.01	17.7	3.58 ± 0.12
J0256+4405 ^c	02:56:35.153	+44:05:27.363	18170 ± 350	5.56 ± 0.06	0.22 ± 0.02	15.8	1.40 ± 0.04
J0450–0145 ^c	04:50:13.108	–01:45:48.150	9560 ± 140	5.58 ± 0.06	0.19 ± 0.02	17.7	0.91 ± 0.11
J0501–2312 ^c	05:01:29.865	–23:12:04.397	21440 ± 330	7.21 ± 0.05	0.36 ± 0.01	18.0	1.64 ± 0.10
J0517–1153 ^c	05:17:24.974	–11:53:25.849	16650 ± 300	5.96 ± 0.06	0.19 ± 0.02	16.2	1.47 ± 0.04
J0545–1902	05:45:45.301	–19:02:45.499	22850 ± 340	7.34 ± 0.05	0.40 ± 0.02	17.3	2.59 ± 0.07
J0725–1245	07:25:27.362	–12:45:46.824	21920 ± 420	7.42 ± 0.06	0.42 ± 0.02	18.9	1.51 ± 0.25
J1121+6052 ^a	11:21:57.163	+60:52:10.265	11690 ± 170	5.41 ± 0.05	0.19 ± 0.01	16.0	1.33 ± 0.04
J1129+4715 ^c	11:29:14.162	+47:15:01.726	11610 ± 170	5.32 ± 0.05	0.19 ± 0.01	16.1	1.18 ± 0.04
J1240–0958	12:40:32.501	–09:58:59.603	14020 ± 280	5.24 ± 0.06	0.20 ± 0.02	19.0	1.30 ± 0.30
J1255–1853	12:55:39.147	–18:53:32.101	11270 ± 200	5.25 ± 0.06	0.19 ± 0.01	17.8	0.55 ± 0.13
J1459–1920	14:59:02.159	–19:20:33.552	8740 ± 130	5.66 ± 0.07	0.26 ± 0.02	18.1	0.71 ± 0.16
J1506–1125	15:06:12.345	–11:25:11.994	(22050 ± 320)	(7.44 ± 0.05)	(0.43 ± 0.02)	17.0	2.42 ± 0.10
J1526–2711 ^c	15:26:01.115	–27:11:56.660	17460 ± 260	7.31 ± 0.05	0.37 ± 0.02	18.3	1.61 ± 0.18
J1553+6736 ^c	15:53:28.008	+67:36:10.560	9610 ± 150	6.11 ± 0.11	0.22 ± 0.04	16.5	2.36 ± 0.04
J1555+1007 ^c	15:55:15.894	+10:07:24.851	13340 ± 220	7.32 ± 0.05	0.35 ± 0.02	18.2	2.52 ± 0.15
J1657–0417	16:57:24.888	–04:17:22.348	17750 ± 270	6.85 ± 0.05	0.27 ± 0.02	18.3	2.04 ± 0.18
J1808+2723	18:08:38.994	+27:23:12.216	10630 ± 270	6.35 ± 0.29	0.22 ± 0.04	15.5	2.82 ± 0.03
J1812+0525 ^b	18:12:38.471	+05:25:29.868	8960 ± 130	5.96 ± 0.08	0.28 ± 0.03	18.9	0.85 ± 0.26
J1832+2031 ^c	18:32:36.539	+20:31:08.202	19080 ± 290	6.74 ± 0.05	0.29 ± 0.03	17.6	1.61 ± 0.08
J2013–1310 ^c	20:13:53.498	–13:10:41.750	11200 ± 190	7.42 ± 0.06	0.37 ± 0.02	18.7	2.21 ± 0.25
J2049+3351 ^b	20:49:51.274	+33:51:53.126	17500 ± 500	5.85 ± 0.05	...	18.7	0.51 ± 0.16
J2102–4145a ^a	21:02:20.456	–41:45:01.736	12700 ± 500	7.20 ± 0.05	0.32 ± 0.01	15.8	6.07 ± 0.04
J2102–4145b ^a	21:02:20.456	–41:45:01.736	13400 ± 500	7.45 ± 0.05	0.39 ± 0.01	...	6.07 ± 0.04
J2243–4511	22:43:27.479	–45:11:18.404	15880 ± 230	7.04 ± 0.05	0.29 ± 0.01	17.4	2.57 ± 0.09
J2303–2614 ^{a,c}	23:03:23.542	–26:14:59.917	11280 ± 160	5.43 ± 0.05	0.18 ± 0.01	13.8	3.12 ± 0.02

^a Photometric variability: TESS high-cadence

^b Photometric variability: ZTF

^c Pelisoli & Vos (2019) ELM white dwarf candidate

Table 1. White dwarf parameters determined through optical spectroscopy for the 28 new binaries identified in this work. Our reported atmospheric parameters T_{eff} and $\log g$ include the external uncertainties of $\sigma_{T_{\text{eff}}} = 1.4\%$ and $\sigma_{\log g} = 0.042$ dex from Liebert et al. (2005). Binaries which show photometric variability in the TESS 2–minute cadence or ZTF data archives are marked. We apply 3D corrections using the equations from Tremblay et al. (2015) for objects cooler than $T_{\text{eff}} \approx 10000$ K. The atmospheric parameter values for J1506–1125 displayed in this table are based on single-star models. We describe our multi-component modeling to J1506–1125 in Section 6, which does not identify a unique solution.

Object Name	P (days)	K (km s $^{-1}$)	γ (km s $^{-1}$)	M_2 (M $_{\odot}$)	τ_{merge} (Gyr)	Disk
J0135+2359	1.177655 ± 0.009923	178.9 ± 6.4	-35.7 ± 6.2	$> 1.02 \pm 0.09$	$< 371.4 \pm 71.7$	1
J0155-4148	0.343865 ± 0.000317	220.4 ± 3.7	-4.0 ± 2.9	$> 0.67 \pm 0.03$	$< 18.1 \pm 1.6$	1
J0215+0155 ^{a,c}	0.387941 ± 0.000001	186.4 ± 1.5	-49.4 ± 1.1	$> 0.58 \pm 0.02$	$< 21.7 \pm 1.4$	0
J0221+1710 ^{b,c}	0.061288 ± 0.000020	347.9 ± 4.2	35.3 ± 3.7	0.58 ± 0.02	0.17 ± 0.01	1
J0256+4405 ^c	0.261260 ± 0.000087	243.7 ± 3.8	28.1 ± 2.9	$> 0.68 \pm 0.03$	$< 8.6 \pm 0.8$	1
J0450-0145 ^c	0.192169 ± 0.000040	260.2 ± 3.3	65.5 ± 2.9	$> 0.61 \pm 0.02$	$< 4.7 \pm 0.5$	1
J0501-2312 ^c	0.086593 ± 0.001156	105.1 ± 5.1	6.3 ± 7.2	$> 0.14 \pm 0.01$	$< 1.1 \pm 0.1$	1
J0517-1153 ^c	0.250521 ± 0.000001	309.7 ± 3.1	53.5 ± 2.6	$> 1.07 \pm 0.04$	$< 6.3 \pm 0.7$	1
J0545-1902	0.144472 ± 0.000684	134.7 ± 5.4	146.1 ± 5.7	$> 0.25 \pm 0.02$	$< 2.4 \pm 0.2$	1
J0725-1245	0.106135 ± 0.000061	79.6 ± 5.0	90.4 ± 3.2	$> 0.12 \pm 0.01$	$< 2.0 \pm 0.2$	1
J1121+6052 ^a	0.084511 ± 0.000013	183.5 ± 2.6	-15.7 ± 2.2	$> 0.20 \pm 0.01$	$< 1.3 \pm 0.1$	1
J1129+4715 ^c	0.238823 ± 0.000032	185.8 ± 4.4	40.9 ± 3.0	$> 0.37 \pm 0.02$	$< 12.4 \pm 0.7$	1
J1240-0958	0.400383 ± 0.002945	209.8 ± 6.1	23.9 ± 3.3	$> 0.65 \pm 0.04$	$< 30.3 \pm 3.2$	1
J1255-1853	0.363739 ± 0.001501	230.8 ± 6.2	-15.2 ± 29.5	$> 0.73 \pm 0.04$	$< 22.6 \pm 1.5$	1
J1459-1920	0.151990 ± 0.000030	287.8 ± 7.4	45.6 ± 5.0	$> 0.70 \pm 0.04$	$< 1.7 \pm 0.1$	0
J1506-1125	0.032320 ± 0.000390	167.5 ± 4.3	43.5 ± 2.8	$> 0.18 \pm 0.01$	$< 0.056 \pm 0.003$	1
J1526-2711 ^c	0.027982 ± 0.000439	336.0 ± 5.6	8.4 ± 4.8	$> 0.40 \pm 0.02$	$< 0.021 \pm 0.001$	1
J1553+6736 ^c	0.174522 ± 0.000431	91.6 ± 5.4	10.9 ± 6.1	$> 0.12 \pm 0.01$	$< 12.4 \pm 2.3$	1
J1555+1007 ^c	0.298037 ± 0.000877	148.5 ± 6.7	-51.4 ± 3.7	$> 0.38 \pm 0.03$	$< 13.0 \pm 1.0$	1
J1657-0417	0.083954 ± 0.000441	289.4 ± 8.8	-69.8 ± 21.3	$> 0.50 \pm 0.03$	$< 0.44 \pm 0.04$	1
J1808+2723	0.098787 ± 0.000053	187.2 ± 3.0	-69.3 ± 1.9	$> 0.24 \pm 0.02$	$< 1.4 \pm 0.2$	1
J1812+0525 ^b	0.059847 ± 0.000083	373.3 ± 6.2	-139.6 ± 4.7	$0.73^{+0.05}_{-0.04}$	0.13 ± 0.01	0
J1832+2031 ^c	0.046641 ± 0.000002	335.2 ± 4.2	-37.4 ± 3.3	$> 0.47 \pm 0.02$	$< 0.090 \pm 0.009$	1
J2013-1310 ^c	0.061618 ± 0.000597	300.9 ± 6.5	-40.2 ± 6.3	$> 0.51 \pm 0.02$	$< 0.14 \pm 0.01$	1
J2049+3351 ^b	0.029747 ± 0.000007	513.2 ± 9.5	-3.4 ± 7.7	1
J2102-4145a ^a	0.117631 ± 0.003244	227^{+8}_{-6}	$-7.9^{+7.1}_{-5.8}$...	$< 0.74 \pm 0.02$	1
J2102-4145b ^a	0.117631 ± 0.003244	186^{+8}_{-7}	$-18.7^{+6.2}_{-7.0}$...	$< 0.74 \pm 0.02$	1
J2243-4511	0.109479 ± 0.000043	249.4 ± 4.9	6.0 ± 3.7	$> 0.46 \pm 0.02$	$< 0.89 \pm 0.04$	1
J2303-2614 ^{a,c}	0.118195 ± 0.000032	302.9 ± 2.3	-17.1 ± 2.1	$> 0.58 \pm 0.01$	$< 1.4 \pm 0.1$	1

^a Photometric variability: TESS high-cadence^b Photometric variability: ZTF^c Pelisoli & Vos (2019) ELM white dwarf candidate**Table 2.** Orbital solutions to the 28 new low mass white dwarf binaries presented in this work.

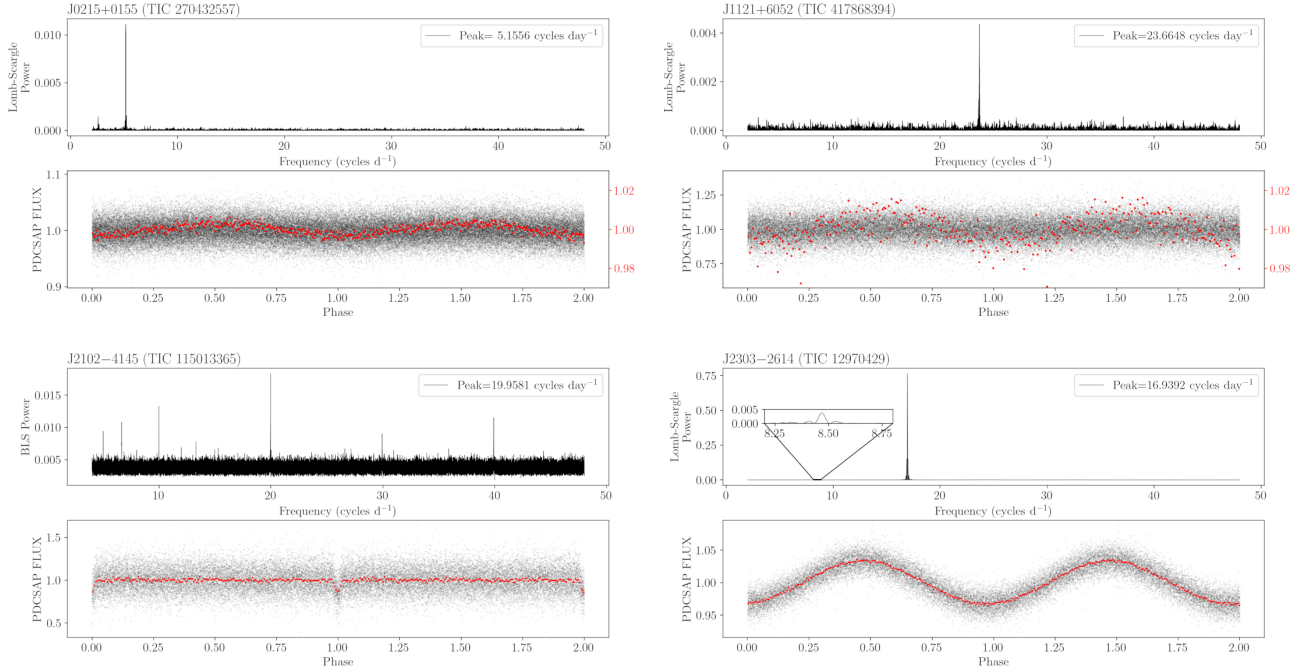


Figure 3. Lomb-Scargle or Box Least Squares (BLS) power spectrum (top) and its TESS 2-minute cadence light curve (bottom) for J0215+0155 (TIC 270432557; upper-left), J1121+6052 (TIC 417868394; upper-right), J2102-4145 (TIC 115013365; lower-left), and J2303-2614 (TIC 12970429; lower-right). Red data points represent the original data binned by 100. We re-scaled the binned data of J0215+0155 and J1121+6052 to emphasize the variability seen at the 1% level.

180 K and $\log g = 5.34 \pm 0.05$, corresponding to white dwarf with mass $M_1 = 0.29 \pm 0.02 M_\odot$ based on the halo metallicity models for He-core white dwarfs from Istrate et al. (2016). With the velocity semi-amplitude known and orbital period known, we used the binary mass function,

$$\frac{(M_2 \sin i)^3}{(M_1 + M_2)^2} = \frac{PK^3}{2\pi G} \quad (1)$$

to estimate the minimum companion mass $M_{2,\min} = 0.59 \pm 0.02 M_\odot$.

We find three sectors of TESS 2-minute cadence data for J0215+0155 (TIC 270432557). Our Lomb Scargle algorithm identifies weak ($\sim 1\%$ level) periodic variability at $f_{\text{TESS}} = 5.1556 \text{ cycles d}^{-1}$, equal to half of the orbital period determined through radial velocity measurements. Figure 3 (upper-left) displays the phase-folded TESS light curve of J0215+0155 and its Lomb Scargle power spectrum. A smaller peak can be seen in the power spectrum at the true orbital frequency of the system. The dominant frequency at 5.1556 cycles d^{-1} is likely caused by tidal distortions in the compact binary. Detailed high-precision follow-up light curve analysis may help place constraints on the orbital inclination and mass ratio of this binary, (see, for example, Hermes et al. 2014).

J0221+1710

We obtained 19 radial velocity measurements of J022110.832+171049.182 (J0221+1710; GAIA DR3 79808158877017216), resulting in orbital parameters $P_{\text{RV}} = 1.4709 \pm 0.0005 \text{ h}$, $K = 347.9 \pm 4.2 \text{ km s}^{-1}$, $\gamma = 35.3 \pm 3.7 \text{ km s}^{-1}$. With precise Gaia astrometry, we estimated Galactic space velocities $[U, V, W] = [-40.4 \pm 1.8, -4.8 \pm 1.6, 7.5 \pm 1.7] \text{ km s}^{-1}$, which are well within the 2σ velocity ellipsoid for the Galactic disk.

Our best-fitting pure-hydrogen atmospheric parameters to J0221+1710 are $T_{\text{eff}} = 13,400 \pm 200 \text{ K}$ and $\log g = 7.01 \pm 0.04$, corresponding to a white dwarf with mass $M_1 = 0.27 \pm 0.01 M_\odot$, based on the $Z = 0.02$ model tracks of Istrate et al. (2016).

Our BLS periodicity search on the ZTF DR13 data archive identified periodic $\Delta m \approx 0.2$ mag eclipses at $P_{\text{ZTF,BLS}} = 88.2508 \text{ min}$ (1.4708 h), in agreement with our orbital period obtained through radial velocity measurements.

We obtained high-speed g - and r -band photometry using the McDonald 2.1-meter telescope on UT 20221001 and UT 20221002. Our observations cover three eclipses in each filter. We used EXPTIME = 10 s, resulting in five mid-eclipse data points and four data points during the ingress or egress per eclipse for the ≈ 90 s eclipse duration.

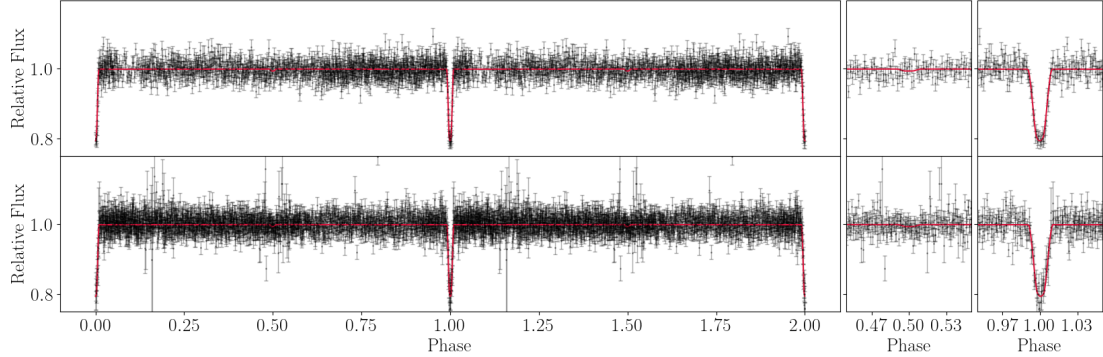


Figure 4. McDonald 2.1-meter *g*-band (top) and *r*-band (bottom) light curves of J0221+1710. Best-fitting LCURVE models are overplotted in red. We provide zoomed-in subplots showing the regions surrounding the primary and secondary eclipses.

	J0221 + 1710	J1812 + 0525	J2049 + 3351
q	...	0.41 ± 0.03	0.39 ± 0.2
i ($^{\circ}$)	89.0 ± 0.2	75^{+2}_{-5}	74^{+3}_{-2}
R_1/a	0.045 ± 0.001	0.20 ± 0.01	0.31 ± 0.05
R_2/a	0.020 ± 0.001	...	$0.06^{+0.03}_{-0.02}$
$T_{\text{eff},1}$ (K)	13400 ± 180	8900 ± 100	23200^{+4900}_{-4300}
$T_{\text{eff},2}$ (K)	$\lesssim 6400$...	35400^{+9700}_{-8600}

Table 3. System parameters for J0221+1710, J1812+0525, and J2049+3351, obtained through light curve modeling with LCURVE as described in the text.

We modeled the geometry of the binary by simultaneously fitting the *g*- and *r*-band light curves using LCURVE (Copperwheat et al. 2010), fitting for the component radii ($r_i = \frac{R_i}{a}$) and the temperature of the companion ($T_{\text{eff},2}$). We fixed the orbital period to the value obtained from our ZTF BLS analysis and used the results from our spectroscopic follow-up ($T_{\text{eff},1}$, $\log g_1$, and K_1) as Gaussian priors to our light curve modeling. We interpolated over the grid of gravity darkening and quadratic limb darkening coefficients from Claret et al. (2020) for our primary star based on our spectroscopic values and used values for a companion with $T_{\text{eff},2} = 10,000$ K and $\log g_2 = 8.0$.

The most probable system parameters from our light curve fitting are $R_1 = 0.028 \pm 0.001$ R $_{\odot}$, $R_2 = 0.012 \pm 0.001$ R $_{\odot}$, $i = 89.0 \pm 0.2^{\circ}$, and $T_{\text{eff},2} = 5200^{+400}_{-500}$ K. However, given the quality of our McDonald *r*-band light curve data during the eclipse, we adopt the 3-sigma upper limit to the temperature of the companion. Our most probable model parameters are summarized in Table 3. Figure 4 displays our phase-folded McDonald 2.1-

meter *g*- (top) and *r*-band (bottom) light curves with the best-fitting model over-plotted in red.

With the inclination and radial velocity semi-amplitude known, we used the binary mass function to calculate the companion mass $M_2 = 0.58 \pm 0.02$ M $_{\odot}$, corresponding to radius $R_2 = 0.0129$ R $_{\odot}$, in agreement with the radius estimate from our light curve modeling.

We similarly fit our eclipsing *g*- and *r*-band light curves for J0221+1710 separately using JKTEBOP (Southworth et al. 2004; Southworth 2013) to confirm the consistency of our LCURVE solution. We fit for the sum and ratio of the component radii, the inclination, and the surface brightness ratio. We performed 10,000 Monte Carlo iterations, which returned a solution degenerate in inclination ($88.6 \pm 0.2^{\circ}$ and $87.9 \pm 0.2^{\circ}$). The most probable degenerate solution agrees well with our LCURVE results, returning: $R_1 = 0.029 \pm 0.001$ R $_{\odot}$, $R_2 = 0.013 \pm 0.001$ R $_{\odot}$, $i = 88.6 \pm 0.2^{\circ}$, and $T_{\text{eff},2} \approx 6200$ K. We report our simultaneous *g*- and *r*-band solution from the LCURVE solution as the true system parameters of J0221+1710.

With the individual component masses, orbital period, and orbital inclination known, we estimated the gravitational wave strain using the equation

$$h_c = 3.4 \times 10^{-23} \frac{\mathcal{M}^{5/3} \sqrt{\cos^4 i + 2 \cos^2 i + 1}}{P^{2/3} d}, \quad (2)$$

where \mathcal{M} is the chirp mass, P is the period in days, and d is the distance in kpc (Timpano et al. 2006; Roelofs et al. 2007). We multiplied by $\sqrt{(4 \text{ yr}) f_{\text{GW}}}$ to account for the increased signal after a 4-year LISA mission. Our estimated gravitational wave strain for J0221+1710 is $h_c = (2.87 \pm 0.14) \times 10^{-20}$. Additionally, we estimated the orbital decay due to gravitational wave emission using the equation

$$\dot{P} = \frac{96}{5} \left(\frac{G \mathcal{M}}{P} \right)^{5/3} \frac{2\pi}{c^5}, \quad (3)$$

resulting in $\dot{P} = (3.86 \pm 0.14) \times 10^{-14} \text{ s s}^{-1}$, which corresponds to an eclipse timing offset of $\Delta T_0 \approx -3.6 \pm 0.1 \text{ s}$ after 10 years.

J1121+6052

Our 26 radial velocity measurements of J112157.163+605210.265 (J1121+6052; GAIA DR3 861011995046220544) return best-fitting orbital parameters $P_{\text{RV}} = 2.0283 \pm 0.0003 \text{ h}$, $K = 183.5 \pm 2.6 \text{ km s}^{-1}$, and $\gamma = -15.7 \pm 2.2 \text{ km s}^{-1}$. We calculated the Galactic space velocities $[U, V, W] = [56.7 \pm 1.4, -10.2 \pm 1.5, 23.4 \pm 1.4] \text{ km s}^{-1}$, consistent with a short-period binary in the disk.

Our pure-hydrogen atmosphere fits to the summed zero-velocity spectrum of J1121+6052 resulted in atmospheric parameters $T_{\text{eff}} = 11,690 \pm 170 \text{ K}$ and $\log g = 5.41 \pm 0.05$, which suggests white dwarf mass $M_1 = 0.19 \pm 0.01 M_{\odot}$ based on the $Z = 0.02$ model tracks of [Istrate et al. \(2016\)](#).

We find a weak periodic signal in the TESS 2-minute cadence data through our Lomb-Scargle periodicity search of J1121+6052 (TIC 417868394). The TESS light curve shows periodic variability at the 1% level with frequency $f_{\text{TESS}} = 23.6649 \text{ cycles d}^{-1}$ ($P_{\text{TESS}} = 1.0142 \text{ h}$); half the period obtained through radial velocity measurements. We display the phase-folded TESS 2-minute cadence light curve in Figure 3 (upper-right). J1121+6042 is in a relatively isolated field, with no nearby bright stars to heavily dilute the TESS light curve. We do not recover this weak periodic signal in the available ground-based ZTF data.

J1506–1125

We obtained 31 radial velocity measurements for J150612.345–112511.994 (J1506–1125; Gaia DR3 6312837970697953920). Our best-fitting circular orbit fits suggest orbital parameters $P_{\text{RV}} = 0.7757 \pm 0.0094 \text{ h}$, $K = 167.5 \pm 4.3 \text{ km s}^{-1}$, and $\gamma = 43.5 \pm 2.8 \text{ km s}^{-1}$. J1506–1125 is likely a disk object with Galactic space velocities $[U, V, W] = [41.8 \pm 1.6, -7.3 \pm 1.5, 13.3 \pm 1.4] \text{ km s}^{-1}$.

Our pure-hydrogen model atmosphere fits to the summed zero-velocity spectrum result in best-fitting atmospheric parameters $T_{\text{eff}} = 22,050 \pm 320 \text{ K}$ and $\log g = 7.44 \pm 0.05$, which corresponds to a white dwarf with mass $M_1 = 0.43 \pm 0.02 M_{\odot}$ based on disk-metallicity models of [Althaus et al. \(2013\)](#). Our radial velocity measurements suggest a minimum companion mass $M_{2,\min} = 0.18 \pm 0.01 M_{\odot}$, significantly below the mass of the visible star.

Interestingly, our distance estimates suggest that J1506–1125 is over-luminous when compared to our

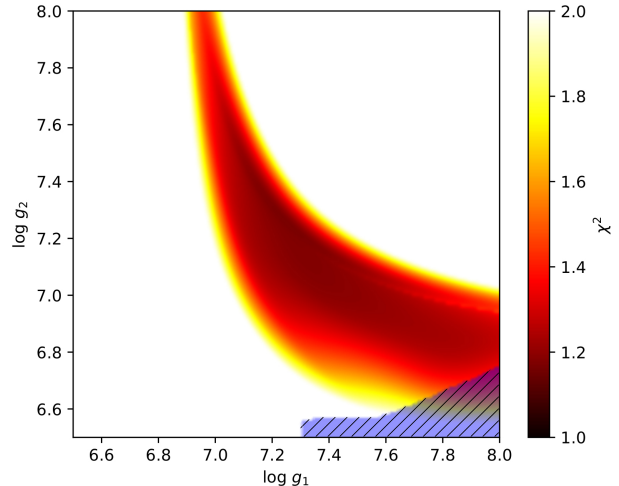


Figure 5. Normalized χ^2 distribution from our fits to the combined SED and optical spectroscopy for J1506–1125, as a function of $\log g_1$ and $\log g_2$. The hatched blue region represents the region of parameter space excluded by constraints from the binary mass function.

single-star SED models, which suggests our single-star atmospheric model parameters may be inaccurate due to significant contribution to the system light from a companion. However, given the relatively low radial velocity semi-amplitude ($K = 167.5 \pm 4.3 \text{ km s}^{-1}$), we are not able to resolve individual absorption components in our Magellan 6.5-meter optical spectrum with $\approx 1.0 \text{ \AA}$ resolution, if they are present.

We performed simultaneous model atmosphere fits to the SED and median-combined optical spectrum of J1506–1125, including contribution from two components in a binary (see [Bédard et al. 2017](#); [Kilic et al. 2020](#), for the details of the method). The SED was built from the available GALEX (NUV; [Martin et al. 2005](#)), SkyMapper (uvgriz; [Onken et al. 2019](#)), Pan-STARRS (grizy; [Chambers et al. 2016](#)), 2MASS (JHK_s; [Skrutskie et al. 2006](#)), and AllWISE (W1; [Wright et al. 2010](#); [Mainzer et al. 2011](#)) photometry, and dereddened using the extinction maps of [Schlafly & Finkbeiner \(2011\)](#). Figure 5 shows the resulting χ^2 distribution plot as a function of $\log g_1$ and $\log g_2$, with the region of parameter space excluded by constraints from the binary mass function shaded in blue. Dark regions indicate the regions with the most probable system parameters based on our fits.

Because we do not resolve individual absorption components in our optical spectrum, we are unable to identify a unique solution to describe the atmospheric parameters of the components of J1506–1125. Figure 6 displays an example fit near the center of the dark region, defined by $T_{\text{eff},1} = 23,300 \text{ K}$, $\log g_1 = 7.30$, $T_{\text{eff},2} = 18,300 \text{ K}$ and $\log g_2 = 7.15$, corresponding to

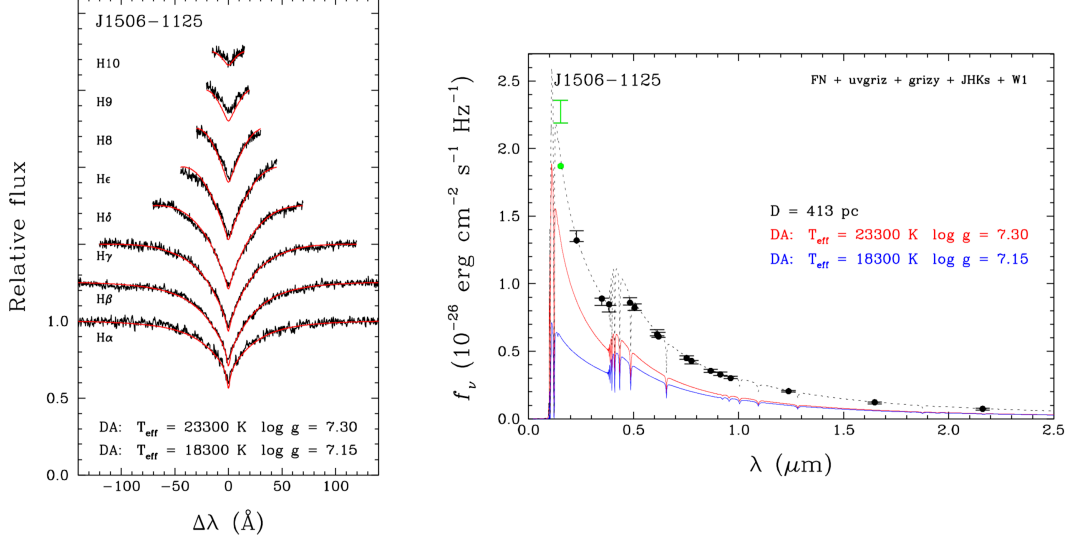


Figure 6. Example model-atmosphere fit to the spectrum (left) and SED (right) of J1506–1125 including contributions from two DA white dwarfs. In the left panel, the observed and predicted Balmer lines are shown as black and red lines, respectively. In the right panel, the observed and predicted average fluxes are displayed as error bars and filled circles, respectively; for reference, the red and blue lines show the individual contributions of the components to the total monochromatic model flux, which is displayed as a black dotted line. The GALEX FUV photometry measurement (green) is excluded from our SED fit. This fit does not represent a unique solution (see text).

masses $M_1 = 0.40 M_{\odot}$ and $M_2 = 0.33 M_{\odot}$ based on He-core cooling tracks of Althaus et al. (2013). However, the extremes of our probable parameter space allow for solutions at $[(T_{\text{eff},1}, T_{\text{eff},2}), (\log g_1, \log g_2), (M_1, M_2)] = [(22,000 \text{ K}, 18,100 \text{ K}), (7.05, 7.55), (0.34 M_{\odot}, 0.43 M_{\odot})]$ and $[(27,300 \text{ K}, 17,900 \text{ K}), (7.80, 6.90), (0.54 M_{\odot}, 0.28 M_{\odot})]$, where we used C/O-core cooling tracks of Bédard et al. (2020) for the relatively massive $0.54 M_{\odot}$ solution.

We find no TESS Full-Frame image data, 2-minute cadence data, or 20-second cadence data for J1506–1125 up to sector 56. Our Lomb-Scargle and BLS algorithms do not identify periodic photometric variability in the public ZTF DR13 data archive.

J1812+0525

The orbital period of J181238.471+052529.868 (J1812+0525; Gaia DR3 4471573464995153280) was constrained through its periodic photometric variability identified in our search of the public ZTF data archive. Our Lomb Scargle periodogram identified periodic photometric variability at $P_{\text{ZTF}} = 43.1 \text{ min}$.

We obtained a single follow-up spectrum on 2022 June 03 to confirm its nature. We then completed its orbital solution with seven additional back-to-back spectra during the following night. Figure 7 (left) displays our orbital solution for J1812+0525. Our best-fitting radial velocity solution finds velocity semi-amplitude $K = 373.3 \pm 6.2 \text{ km s}^{-1}$, systemic velocity $\gamma = -139.6 \pm 4.7 \text{ km s}^{-1}$, and orbital period $P_{\text{RV}} = 1.436 \pm 0.002 \text{ h}$

($86.2 \pm 0.1 \text{ min}$), in good agreement with the half-period identified from the ZTF data. We use the precise Gaia DR3 astrometry, together with our radial velocity information, to estimate its Galactic velocities $[U, V, W] = [-92.9 \pm 2.3, -87.4 \pm 2.8, -1.1 \pm 2.4] \text{ km s}^{-1}$, which suggests that J1812+0525 is a short-period binary in the Galactic Halo.

We fit the summed zero-velocity spectrum with pure-hydrogen model atmospheres and obtained best-fitting atmospheric parameters $T_{\text{eff},0} = 9300 \pm 120 \text{ K}$ and $\log g_0 = 6.11 \pm 0.05$. Because this is a cool object, we corrected its atmospheric solution for 3D effects using equations provided in Tremblay et al. (2015), resulting in corrected atmospheric parameters $T_{\text{eff}} = 8960 \pm 130 \text{ K}$ and $\log g = 5.96 \pm 0.08$, corresponding to a primary mass $M_1 = 0.28 \pm 0.03 M_{\odot}$ based on the halo-metallicity models tracks of Istrate et al. (2016).

We used the McDonald Observatory 2.1-meter telescope to confirm photometric variability at $P = 43.4 \text{ min}$, roughly consistent with the half-period seen in the public ZTF data. However, our data quality is too poor to reasonably constrain orbital parameters through photometric fitting.

We instead modelled the ZTF DR16 g - and r -band data simultaneously using LCURVE. Our free parameters included the mass ratio ($q = \frac{M_1}{M_2} < 1.0$), scaled primary star radius ($r_1 = \frac{R_1}{a}$), orbital inclination (i), primary star effective temperature ($T_{\text{eff},1}$), time of superior conjunction (t_0), and the velocity scale (the sum of the unprojected orbital speeds). We fixed the gravity

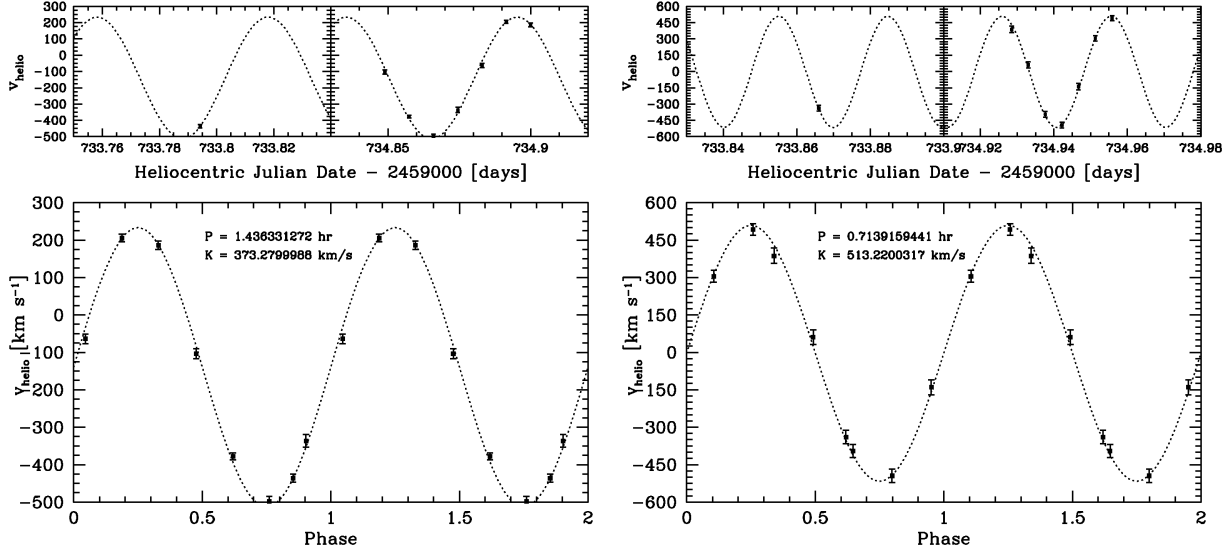


Figure 7. Orbital solutions for J1812+0525 (left) and J2049+3351 (right).

and quadratic limb-darkening coefficients to values from Claret et al. (2020) for a $T_{\text{eff},1} = 9000 \text{ K}$, $\log g_1 = 6.0$ primary with a $T_{\text{eff},2} = 5500 \text{ K}$, $\log g_1 = 8.0$ companion and assign Gaussian priors based on our spectroscopic values for $T_{\text{eff},1}$, $\log g_1$, and K_1 . The most-probable system parameters based on our light curve modelling are $q = 0.42 \pm 0.03$, $r_1 = 0.20 \pm 0.01$, $i = 75^{+2}_{-5} \text{ }^\circ$, and $T_{\text{eff},1} = 8900 \pm 100 \text{ K}$. These parameters are summarized in Table 3. With constraints from our radial velocity measurements, this corresponds to an $M_1 = 0.30 \pm 0.03 \text{ M}_\odot$ primary star with an $M_2 = 0.73^{+0.05}_{-0.04} \text{ M}_\odot$ companion.

J2049+3351

The orbital period of J204951.274+335153.126 (J2049+3351; Gaia DR3 1869111286948848128) was constrained through its periodic photometric variability identified in our search of the public ZTF data archive. Our Lomb Scargle algorithm identified strong variability at $P_{\text{ZTF}} = 21.6 \text{ min}$ with amplitude $A \approx 0.07 \text{ mag}$.

We obtained a single follow-up spectrum on 2022 June 03 to confirm its nature and completed its orbital solution with seven additional back-to-back spectra on the following night. Figure 7 (right) displays our orbital solution for J2049+3351. Our best-fitting radial velocity solution yields velocity semi-amplitude $K = 513.2 \pm 9.5 \text{ km s}^{-1}$, systemic velocity $\gamma = -3.4 \pm 7.7 \text{ km s}^{-1}$, and orbital period $P_{\text{RV}} = 0.7139 \pm 0.0002 \text{ h}$ ($42.834 \pm 0.012 \text{ min}$), in good agreement with the half-period identified from the ZTF data. The Galactic space velocities, $[U, V, W] = [-9.8 \pm 2.4, -8.1 \pm 2.6, 13.4 \pm 2.3] \text{ km s}^{-1}$, place J2049+3351 in the Galactic disk.

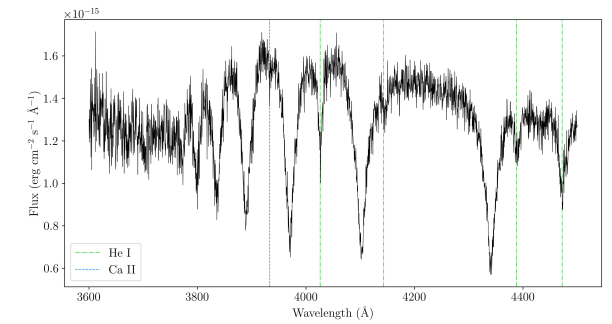


Figure 8. Co-added MMT optical spectrum of J2049+3351. In addition to the dominant Hydrogen Balmer absorption, strong neutral Helium absorption features (green dash-dot lines) can be seen at 4472 Å, 4388 Å, 4143 Å, and 4026 Å, as well as a weak Ca II absorption feature (blue dash lines) at 3933 Å.

J2049+3351 has an interesting optical absorption spectrum, including broad Hydrogen Balmer lines with strong He I absorption at 4472 Å, 4388 Å, 4143 Å, and 4026 Å, as well as a weak Ca II feature at 3933 Å. Our MMT 6.5-meter optical spectrum of J2049+3351 is presented in Figure 8. We note that the individual Hydrogen and Helium absorption lines appear to move in-sync with each other throughout the orbit of the binary.

To fit the co-added spectrum of J2049+3351, we use spectral models which were constructed using a hybrid LTE/NLTE approach described in detail in Przybilla et al. (2011) and Irrgang et al. (2021). The grid of spectral models covers a typical range of hot subdwarf T_{eff} , and $\log g$, up to modest helium abundances (Heber 2023; Irrgang et al. 2021, 2022). Our best-fitting

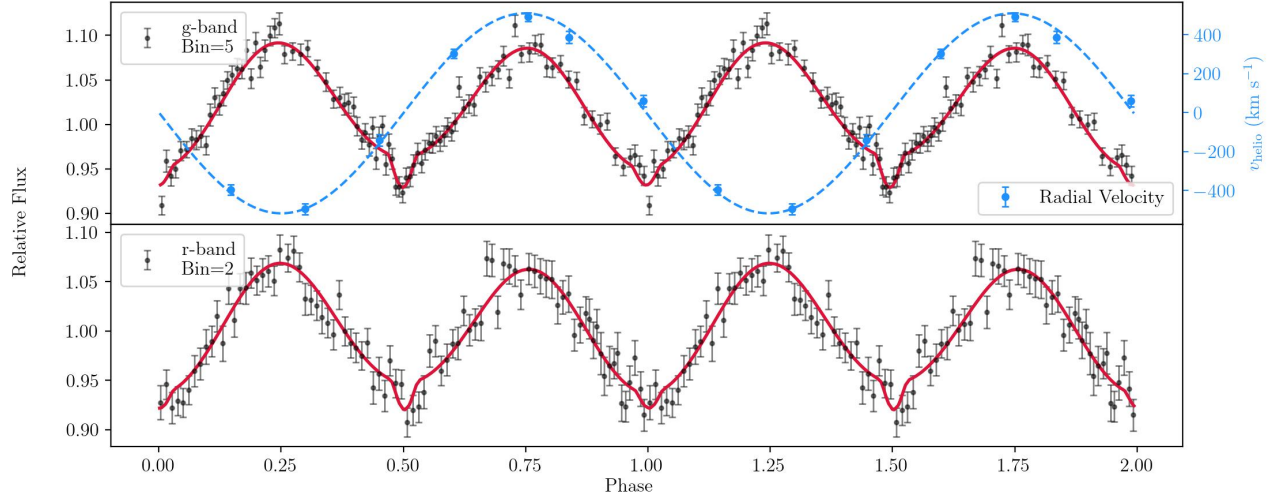


Figure 9. Top: McDonald 2.1-meter *g*-band (top; binned by 5) and *r*-band (bottom; binned by 2) light curves of ZTF J2049+3351. We overplot our radial velocity measurements as blue data points in the top panel.

lutions without rotational broadening fail to reproduce the observed broad Helium absorption lines. We present the best-fitting model atmosphere over-plotted on our optical spectrum in Figure 10.

We obtained 218 min of *g*-band and 108 min of *r*-band high-speed photometry using the McDonald 2.1-meter telescope. We performed a simultaneous multi-band fit to our unbinned light curves using LCURVE. We assign the time of primary conjunction using our radial velocity data and fit for the mass ratio, individual stellar radii, orbital inclination, and effective temperatures.

Our best-fitting model identifies primary and secondary eclipses in the data. However, J2049+3351 is faint (Gaia $G = 18.7$ mag), and our 2.1-meter McDonald light curves are noisy. While the eclipses are not seen in our *r*-band light curve due to the high noise level, a relatively clean secondary-eclipse feature can be seen in the binned *g*-band light curve data and a noisy primary-eclipse feature may be visible in our unbinned *g*-band data. We present our binned and phase-folded McDonald 2.1-meter *g*- and *r*-band light curves in Figure 9 with the most-probable light curve model over-plotted as a red line and radial velocity curve over-plotted in blue.

Our best-fitting model to the McDonald 2.1-meter light curves finds mass ratio $q = \frac{M_1}{M_2} = 0.39 \pm 0.2$, inclination $i = 74 \pm 3^\circ$, $T_{\text{eff},1} = 23,200^{+4900}_{-4300}$ K, $T_{\text{eff},2} = 35,400^{+9700}_{-8600}$ K, $r_1 = \frac{R_1}{a} = 0.31 \pm 0.05$, and $r_2 = \frac{R_2}{a} = 0.06^{+0.03}_{-0.02}$. We summarize these values in Table 3.

Because J2049+3351 is faint, large aperture high-speed photometry will be required to obtain sufficient signal-to-noise to confirm the presence of eclipses. These

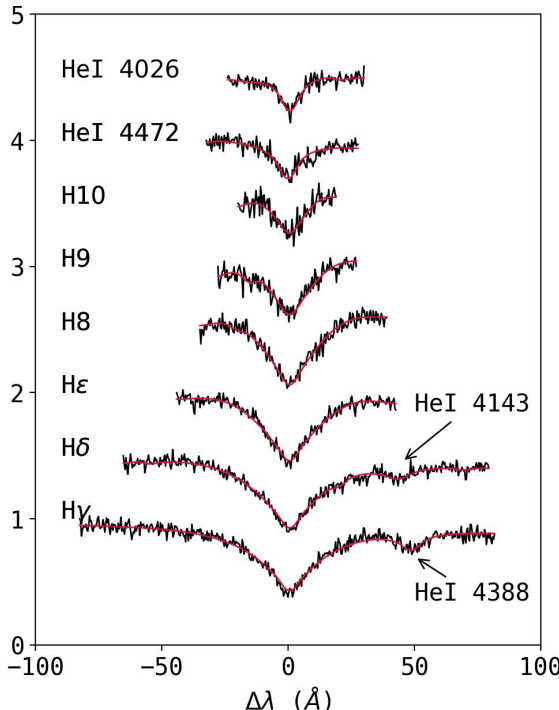


Figure 10. Best fitting spectroscopic model to the optical spectroscopy of J2049+3351, including rotational broadening.

parameters, with their bootstrapped uncertainties, are $T_{\text{eff}} = 17,500 \pm 500$ K, $\log g = 5.85 \pm 0.05$, $\log \frac{H_e}{H} = -0.24 \pm 0.07$, and $v_{\text{rot}} = 260 \pm 60$ km s $^{-1}$. Best-fitting so-

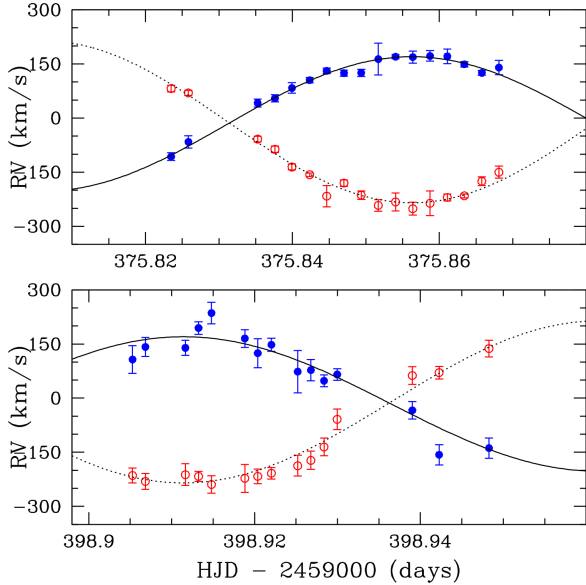


Figure 11. Orbital solutions for each component of the double-lined binary J2102–4145. Top: Magellan 6.5-meter telescope data. Bottom: Gemini South 8.1-meter telescope data. The blue/red points represent the radial velocity measurements for the primary/secondary star.

future observations will be used to place precise constraints on the binary parameters and determine the evolutionary history of J2049+3351.

J2102–4145

J210220.456–414501.736 (J2102–4145; Gaia DR3 6581249825853801984) is a relatively bright (Gaia $G = 15.7$ mag) and nearby ($d_\pi = 165 \pm 1$ pc) eclipsing low mass white dwarf binary. Our 6.5-meter Magellan spectroscopic follow-up observations reveal two nearly-equal depth absorption components, most easily seen in $\text{H}\alpha$. Thus J2102–4145 is now the eighth confirmed double-lined, double-degenerate, eclipsing white dwarf binary published after CSS41177 (J1005+2249; Bours et al. 2014), ZTF J1539+5027 (Burdge et al. 2019), ZTF J1901+5309 Coughlin et al. (2020), and ZTF J0538+1953, ZTF J0722–1839, ZTF J1749+0924, and ZTF J2029+1534 (Burdge et al. 2020).

Because the individual absorption components are roughly equal-depth, obtaining a precise orbital period and individual velocity semi-amplitudes leads to significant period aliases when combining data over multiple nights. Our 55 radial velocity measurements for J2102–4145 provide orbital period constraints with strong period aliases between $P_{\text{RV}} = 2 – 3$ h.

Fortunately, the TESS 2-minute cadence data archive provides a light curve for J2102–4145 (TIC 115013365). Our BLS algorithm identifies periodic eclipses in the TESS light curve with period $P_{\text{BLS}} = 1.2$ h, with

its phase-folded light curve showing a shallow primary eclipse heavily diluted by a bright (Gaia $G = 11.2$ mag) field star roughly $30''$ away. Figure 3 (lower-left) shows the phase-folded TESS 2-minute cadence light curve and its BLS periodogram for J2102–4145.

Given that this is a double-lined spectroscopic binary with nearly-equal depth absorption components, our BLS algorithm will confuse the nearly-equal depth primary and secondary eclipses at the true orbital period with one primary eclipse occurring twice as often. Our BLS algorithm has identified the half-period; the true orbital period of J2102–4145 is therefore $P = 2.4$ h, in agreement with the constraints from our radial velocity analysis.

Using the TESS period, we were able to constrain the orbital solutions for both stars in the binary. Figure 11 displays our best-fitting orbital solution for each star, using data from Magellan and Gemini South. We find $P_{\text{RV}} = 144.3^{+0.4}_{-0.3}$ min, $K_1 = 227 \pm 8$ km s $^{-1}$, $\gamma_1 = -8^{+7}_{-6}$ km s $^{-1}$, $K_2 = 186 \pm 8$ km s $^{-1}$, and $\gamma_2 = -19^{+6}_{-7}$ km s $^{-1}$, corresponding to binary mass ratio $q = 0.82 \pm 0.05$.

Finally, we performed simultaneous model atmosphere fits to the SED and median-combined spectrum of J2102–4145, including the contributions of both components. To avoid significant smearing, our median combined spectrum used four consecutive spectra covering 9% of the orbit, approaching maximum separation. Our fits also made use of the Gaia DR3 parallax measurement and the mass ratio constraint provided by the orbital solution, thanks to which we were able to obtain a unique solution, shown in Figure 12.

Our best-fitting solution suggests that J2102–4145 contains two similar DA white dwarfs with atmospheric parameters $T_{\text{eff},1} = 12,700 \pm 500$ K, $\log g_1 = 7.20 \pm 0.05$, $T_{\text{eff},2} = 13,400 \pm 500$ K, and $\log g_2 = 7.45 \pm 0.05$, corresponding to masses $M_1 = 0.32 M_\odot$ and $M_2 = 0.39 M_\odot$ based on the He-core white dwarf tracks of Althaus et al. (2013), in agreement to within 2σ of the expected values based on the difference in systemic velocities measured from our radial velocity solution.

High-speed light curve follow-up of J2102–4145 will allow for a rare opportunity to directly measure the radii of the individual stars in the binary, independent of model estimates.

J2303–2615

We obtained 34 radial velocity measurements of J230323.542–261459.917 (J2303–2614; Gaia DR3 2382531303846872448), resulting in a best-fitting circular orbit with parameters $P_{\text{RV}} = 2.8367 \pm 0.0008$ h, $K = 302.9 \pm 2.3$ km s $^{-1}$ and $\gamma = -17.1 \pm 2.1$ km s $^{-1}$.

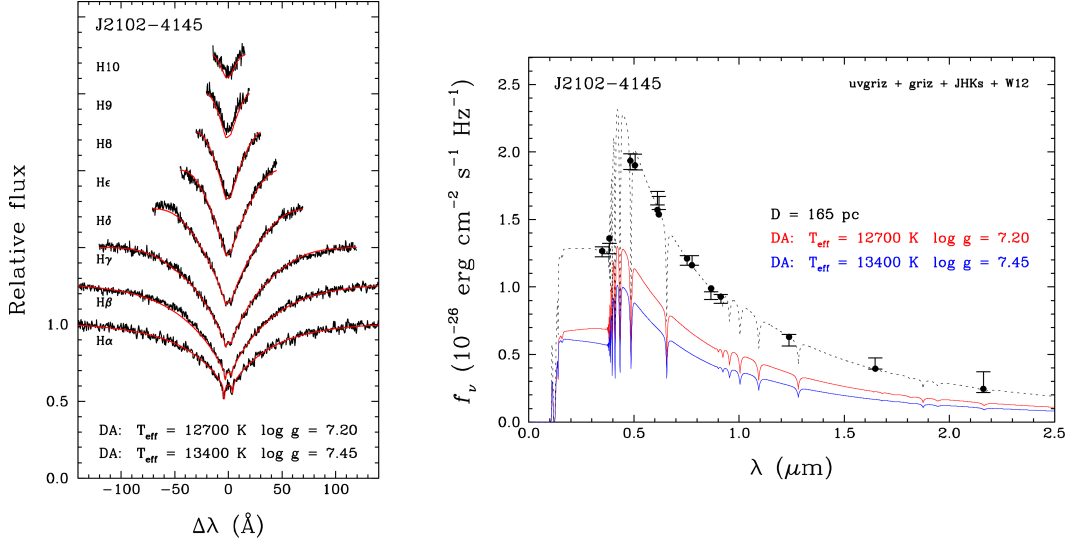


Figure 12. Best simultaneous model-atmosphere fit to the spectrum (left) and SED (right) of J2102–4145 including contributions from two DA white dwarfs. In the left panel, the observed and predicted Balmer lines are shown as black and red lines, respectively. In the right panel, the observed and predicted average fluxes are displayed as error bars and filled circles, respectively; for reference, the red and blue lines show the individual contributions of the components to the total monochromatic model flux, which is displayed as a black dotted line

J2303–2614 is a disk object with $[U, V, W] = [31.1 \pm 1.2, -60.0 \pm 1.4, 18.8 \pm 1.4]$ km s $^{-1}$.

We fit the median-combined zero-velocity spectrum with pure-hydrogen atmosphere models and obtained best-fitting atmospheric parameters $T_{\text{eff}} = 11,280 \pm 170$ K and $\log g = 5.43 \pm 0.05$, corresponding to a white dwarf with mass $M_1 = 0.18 \pm 0.01$ M $_{\odot}$.

Our Lomb-Scargle periodogram identified strong periodic photometric variability in the TESS 2-minute cadence data of J2303–2614 (TIC 12970429) at frequency $f_{\text{TESS}} = 16.9392$ cycles d $^{-1}$ ($P = 1.417$ h), in good agreement with half the orbital period seen in our radial velocity follow-up, suggesting that J2303–2614 is another tidally distorted white dwarf in a compact binary. Figure 3 (lower-right) shows the phase-folded TESS 2-minute cadence light curve and its Lomb Scargle power spectrum. We provide a zoomed-inset plot showing a small, but significant, peak at the true orbital period of this system.

7. DISCUSSION

7.1. Detectable LISA Binaries

General relativity predicts that the orbits of compact binaries decay due to the emission of gravitational waves. Binaries with orbital periods $P \lesssim 6$ h will merge within a Hubble time. The shortest period white dwarf binaries, with periods $P \lesssim 1$ h, will be the dominant source of gravitational wave signal for the Laser Interferometer Space Antenna (LISA; Amaro-Seoane et al. 2017) mission, creating an incoherent noise floor in the LISA sensitivity range at mHz frequencies (Nelemans et

al. 2001; Korol et al. 2017; Li et al. 2020; Amaro-Seoane et al. 2022).

Over 40 compact binaries have been characterized through their electromagnetic radiation and will be individually resolved by LISA, many of which will act as verification binaries for the LISA mission data calibration (see Finch et al. 2022; Kupfer et al. 2023, and references therein). These individually resolvable gravitational wave binaries will provide a multi-messenger approach to studying compact binary evolution through their electromagnetic and gravitational wave emission. We find that two of our 28 new binaries will be detected by LISA within a 4-year mission.

Our single star spectroscopic fits to J1506–1125 suggests that it contains an $M_1 = 0.43 \pm 0.02$ M $_{\odot}$ white dwarf in a $P = 0.7757 \pm 0.0094$ h binary with an $M_2 > 0.18 \pm 0.01$ M $_{\odot}$ companion at a distance of $d_{\pi} = 413 \pm 18$ pc. We used the NASA LISA Detectability Calculator⁷ to estimate its expected LISA signal-to-noise ratio over 4-years of observation to be SNR = 1.9 assuming $i = 90^\circ$, or SNR = 3.7 assuming $i = 60^\circ$. However, our single-component fits to the SED of J1506–1125 suggest significant contribution to the total system light from an unseen companion. Our simultaneous multi-component fits to the available SED and optical spectroscopy of J1506–1125 (discussed in Section 6) suggest a large range of probable stellar parameters for each component. Over this range, we find

⁷ <https://heasarc.gsfc.nasa.gov/lisa/lisatool/>

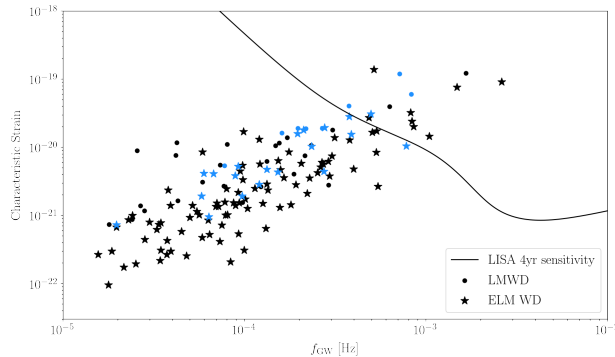


Figure 13. Four-year LISA sensitivity plot including the white dwarf binaries identified as part of the ELM Survey (black) and the 28 new white dwarf binaries from this work (blue). ELM white dwarfs ($M \leq 0.305 M_{\odot}$) are marked as star symbols while low-mass white dwarfs are marked as circles.

signal to noise ratios between $3.9 - 4.7$ assuming $i = 90^\circ$, or $6.1 - 7.3$ assuming $i = 60^\circ$.

J152601.115–271156.660 (J1526–2711; Gaia DR3 6213619999912198144) is a $P = 0.67 \pm 0.01$ h binary containing an $M_1 = 0.37 \pm 0.02 M_{\odot}$ primary with an $M_2 > 0.40 \pm 0.02 M_{\odot}$ companion at a distance $d_{\pi} = 623 \pm 68$ pc. J1526–2711 is a detectable LISA binary with 4-year signal-to-noise $\text{SNR} = 3.3$ assuming $i = 90^\circ$, or $\text{SNR} = 6.4$ assuming $i = 60^\circ$.

We find no photometric variability for either of these binaries in the public ZTF and TESS data archives. LISA detections will provide precise constraints to their orbital inclinations and chip masses, which will be used to directly constrain individual component masses, leading to estimates on the eventual merger outcomes.

Figure 13 displays the LISA 4-year sensitivity curve for the ELM Survey binaries (black) with the 28 new binaries presented here (blue). We calculated the gravitational wave strain for each of our new binaries using Equation 2, assuming $i = 90^\circ$ if orbital inclination was not known through photometric constraints.

7.2. Comparison with other surveys

Pelisoli & Vos (2019) created a catalog of 5672 ELM white dwarf candidates based on Gaia DR2 astrometry with extensive target cuts to remove contamination. We cross-matched our 28 new binaries with the Gaia DR2 ELM white dwarf candidate catalog of Pelisoli & Vos (2019) and find thirteen matches, which we mark in Tables 1 and 2. Many of the remaining binaries not reported as ELM white dwarf candidates in Pelisoli & Vos (2019) were excluded in their color cuts used to remove cataclysmic variables and WD+M binary contaminants.

Wang et al. (2022) used the LAMOST DR8 low resolution spectroscopy to further refine the candidate list

of Pelisoli & Vos (2019) and identified 21 high probability ELM white dwarfs based on spectroscopic fits to the low resolution LAMOST data, including two of the new binaries we present in this work. Wang et al. (2022) identified J0215+0155 with atmospheric parameters $T_{\text{eff}} = 10,540 \pm 40$ K and $\log g = 5.06 \pm 0.07$, significantly lower than the values we find for our combined spectrum. Additionally, the authors identify significant radial velocity variability in two spectra of J1129+4715, with $T_{\text{eff},1} = 11,670 \pm 50$ K, $\log g_1 = 5.31 \pm 0.06$, and $v_{\text{rad},1} = -38.9 \pm 3.0 \text{ km s}^{-1}$ and $T_{\text{eff},2} = 11,150 \pm 90$ K, $\log g_2 = 5.06 \pm 0.02$, and $v_{\text{rad},2} = 94.9 \pm 5.4 \text{ km s}^{-1}$, the first of which is in excellent agreement with the atmospheric parameter estimates from the fits presented in this work.

7.3. Conclusions

This work has identified 28 new low mass white dwarf binaries, bringing the total number of ELM Survey binaries to 148, with 41 located in the southern sky. Interestingly, this work identifies only three halo binaries among our 28 new binaries ($\approx 11\%$). Previous ELM Survey results suggest a significant contribution from halo objects of $\approx 30 - 40\%$ (Gianninas et al. 2015; Brown et al. 2022), likely due to the early ELM Survey target selection being based on photometry from SDSS, which observed at high Galactic latitudes. Additionally, our low fraction of new Halo objects is likely affected by our Gaia-based selection, and in-progress object follow-up, favoring nearby objects with reliable parallax measurements, rather than more distant halo objects.

Large-scale time-domain surveys are an excellent tool for the discovery of photometrically variable systems. Burdge et al. (2020) identified 15 ultra-compact ($P < 1$ h) binaries which show photometric variability in the ZTF data archive. We used the ZTF and TESS data archives to identify photometric variability in seven of our new binaries, including three short period eclipsing binaries. These short-period eclipsing binaries are especially important for determining precise physical parameters of both stars in the binary, which are valuable for binary population studies. Similar upcoming large-scale time-domain surveys, such as BlackGEM (Bloemen et al. 2015) and the Vera C. Rubin Observatory’s Legacy Survey of Space and Time (LSST) program (Ivezić et al. 2019) will enable efficient identification and characterization of white dwarf binaries in the southern sky, which will quickly expand the known population of ELM white dwarf binaries and allow for a more detailed population study of all-sky ELM white dwarf binaries.

ACKNOWLEDGEMENTS

AK acknowledges support from NASA through grant 80NSSC22K0338.

MK acknowledges support from NSF under grants AST-1906379 and AST-2205736, and the NASA under grant 80NSSC22K0479.

TK acknowledges support from the National Science Foundation through grant AST #2107982, from NASA through grant 80NSSC22K0338 and from STScI through grant HST-GO-16659.002-A.

M.A.A. acknowledges support from a Fulbright U.S. Scholar grant co-funded by the Nouvelle-Aquitaine Regional Council and the Franco-American Fulbright Commission. M.A.A. also acknowledges support from a Chrétien International Research Grant from the American Astronomical Society.

We would like to thank Ulrich Heber and Andreas Irrgang for the providing the spectral models for J2049+3351.

We thank the anonymous referee for helpful comments and suggestions that improved the quality of this work.

This work has made use of data from the European Space Agency (ESA) mission *Gaia* (<https://www.cosmos.esa.int/gaia>), processed by the *Gaia* Data Processing and Analysis Consortium (DPAC, <https://www.cosmos.esa.int/web/gaia/dpac/consortium>). Funding for the DPAC has been provided by national institutions, in particular the institutions participating in the *Gaia* Multilateral Agreement.

Based on observations obtained at the international Gemini Observatory, a program of NSF's NOIRLab, which is managed by the Association of Universities for Research in Astronomy (AURA) under a cooperative agreement with the National Science Foundation on behalf of the Gemini Observatory partnership: the National Science Foundation (United States), National Research Council (Canada), Agencia Nacional de Investigación y Desarrollo (Chile), Ministerio de Ciencia, Tecnología e Innovación (Argentina), Ministério da Ciência, Tecnologia, Inovações e Comunicações (Brazil), and Korea Astronomy and Space Science Institute (Republic of Korea).

Based on observations obtained at the Southern Astrophysical Research (SOAR) telescope, which is a joint project of the Ministério da Ciência, Tecnologia e Inovações do Brasil (MCTI/LNA), the US National Science Foundation's NOIRLab, the University of North Carolina at Chapel Hill (UNC), and Michigan State University (MSU).

Observations reported here were obtained at the MMT Observatory, a joint facility of the Smithsonian Institution and the University of Arizona.

The MDM Observatory is operated by Dartmouth College, Columbia University, Ohio State University, Ohio University, and the University of Michigan.

Some of the data presented in this paper were obtained from the Mikulski Archive for Space Telescopes (MAST) at the Space Telescope Science Institute. The specific observations analyzed can be accessed via <https://doi.org/10.17909/ew79-we39>. STScI is operated by the Association of Universities for Research in Astronomy, Inc., under NASA contract NAS5-26555. Support to MAST for these data is provided by the NASA Office of Space Science via grant NAG5-7584 and by other grants and contracts.

This paper includes data collected with the TESS mission, obtained from the MAST data archive at the Space Telescope Science Institute (STScI). Funding for the TESS mission is provided by the NASA Explorer Program. STScI is operated by the Association of Universities for Research in Astronomy, Inc., under NASA contract NAS 5-26555.

Based on observations obtained with the Samuel Oschin 48-inch Telescope at the Palomar Observatory as part of the Zwicky Transient Facility project. ZTF is supported by the National Science Foundation under Grant No. AST-1440341 and a collaboration including Caltech, IPAC, the Weizmann Institute for Science, the Oskar Klein Center at Stockholm University, the University of Maryland, the University of Washington, Deutsches Elektronen-Synchrotron and Humboldt University, Los Alamos National Laboratories, the TANGO Consortium of Taiwan, the University of Wisconsin at Milwaukee, and Lawrence Berkeley National Laboratories. Operations are conducted by COO, IPAC, and UW.

This publication makes use of data products from the Two Micron All Sky Survey, which is a joint project of the University of Massachusetts and the Infrared Processing and Analysis Center/California Institute of Technology, funded by the National Aeronautics and Space Administration and the National Science Foundation.

This publication makes use of data products from the Wide-field Infrared Survey Explorer, which is a joint project of the University of California, Los Angeles, and the Jet Propulsion Laboratory/California Institute of Technology, and NEOWISE, which is a project of the Jet Propulsion Laboratory/California Institute of Technology. WISE and NEOWISE are funded by the National Aeronautics and Space Administration.

The authors acknowledge the High Performance Computing Center⁸ (HPCC) at Texas Tech University for providing computational resources that have con-

tributed to the research results reported within this paper.

This work made use of Astropy:⁹ a community-developed core Python package and an ecosystem of tools and resources for astronomy (Astropy Collaboration et al. 2013, 2018, 2022).

REFERENCES

- Althaus, L. G., Miller Bertolami, M. M., & Córscico, A. H. 2013, *A&A*, 557, A19. doi:10.1051/0004-6361/201321868
- Amaro-Seoane, P., Audley, H., Babak, S., et al. 2017, arXiv:1702.00786
- Amaro-Seoane, P., Andrews, J., Arca Sedda, M., et al. 2022, arXiv:2203.06016
- Astropy Collaboration, Robitaille, T. P., Tollerud, E. J., et al. 2013, *A&A*, 558, A33. doi:10.1051/0004-6361/201322068
- Astropy Collaboration, Price-Whelan, A. M., Sipőcz, B. M., et al. 2018, *AJ*, 156, 123. doi:10.3847/1538-3881/aabc4f
- Astropy Collaboration, Price-Whelan, A. M., Lim, P. L., et al. 2022, *ApJ*, 935, 167. doi:10.3847/1538-4357/ac7c74
- Abazajian, K., Adelman-McCarthy, J. K., Agüeros, M. A., et al. 2003, *AJ*, 126, 2081. doi:10.1086/378165
- Bellm, E. C., Kulkarni, S. R., Graham, M. J., et al. 2019, *PASP*, 131, 018002. doi:10.1088/1538-3873/aaecbe
- Bédard, A., Bergeron, P., & Fontaine, G. 2017, *ApJ*, 848, 11. doi:10.3847/1538-4357/aa8bb6
- Bédard, A., Bergeron, P., Brassard, P., et al. 2020, *ApJ*, 901, 93. doi:10.3847/1538-4357/abafbe
- Bloemen, S., Groot, P., Nelemans, G., et al. 2015, *Living Together: Planets, Host Stars and Binaries*, 496, 254
- Brown, W. R., Kilic, M., Allende Prieto, C., et al. 2010, *ApJ*, 723, 1072. doi:10.1088/0004-637X/723/2/1072
- Brown, W. R., Kilic, M., Allende Prieto, C., et al. 2012, *ApJ*, 744, 142. doi:10.1088/0004-637X/744/2/142
- Brown, W. R., Kilic, M., Allende Prieto, C., et al. 2013, *ApJ*, 769, 66. doi:10.1088/0004-637X/769/1/66
- Brown, W. R., Gianninas, A., Kilic, M., et al. 2016a, *ApJ*, 818, 155. doi:10.3847/0004-637X/818/2/155
- Brown, W. R., Kilic, M., Kenyon, S. J., et al. 2016b, *ApJ*, 824, 46. doi:10.3847/0004-637X/824/1/46
- Brown, W. R., Kilic, M., Kosakowski, A., et al. 2020, *ApJ*, 889, 49. doi:10.3847/1538-4357/ab63cd
- Brown, W. R., Kilic, M., Kosakowski, A., et al. 2022, *ApJ*, 933, 94. doi:10.3847/1538-4357/ac72ac
- Bours, M. C. P., Marsh, T. R., Parsons, S. G., et al. 2014, *MNRAS*, 438, 3399. doi:10.1093/mnras/stt2453
- Burdge, K. B., Coughlin, M. W., Fuller, J., et al. 2019, *Nature*, 571, 528. doi:10.1038/s41586-019-1403-0
- Burdge, K. B., Prince, T. A., Fuller, J., et al. 2020, *ApJ*, 905, 32. doi:10.3847/1538-4357/abc261
- Chambers, K. C., Magnier, E. A., Metcalfe, N., et al. 2016, arXiv:1612.05560. doi:10.48550/arXiv.1612.05560
- Chiba, M. & Beers, T. C. 2000, *AJ*, 119, 2843. doi:10.1086/301409
- Claret, A., Cukanovaite, E., Burdge, K., et al. 2020, *A&A*, 634, A93. doi:10.1051/0004-6361/201937326
- Clemens, J. C., Crain, J. A., & Anderson, R. 2004, *Proc. SPIE*, 5492, 331. doi:10.1117/12.550069
- Copperwheat, C. M., Marsh, T. R., Dhillon, V. S., et al. 2010, *MNRAS*, 402, 1824. doi:10.1111/j.1365-2966.2009.16010.x
- Coughlin, M. W., Burdge, K., Phinney, E. S., et al. 2020, *MNRAS*, 494, L91. doi:10.1093/mnrasl/slaa044
- Finch, E., Bartolucci, G., Chucherko, D., et al. 2022, arXiv:2210.10812
- Gaia Collaboration, Prusti, T., de Bruijne, J. H. J., et al. 2016, *A&A*, 595, A1. doi:10.1051/0004-6361/201629272
- Gaia Collaboration, Brown, A. G. A., Vallenari, A., et al. 2021, *A&A*, 649, A1. doi:10.1051/0004-6361/202039657
- Gaia Collaboration, Vallenari, A., Brown, A. G. A., et al. 2022, arXiv:2208.00211. doi:10.48550/arXiv.2208.00211
- Gianninas, A., Bergeron, P., & Ruiz, M. T. 2011, *ApJ*, 743, 138. doi:10.1088/0004-637X/743/2/138
- Gianninas, A., Dufour, P., Kilic, M., et al. 2014, *ApJ*, 794, 35. doi:10.1088/0004-637X/794/1/35
- Gianninas, A., Kilic, M., Brown, W. R., et al. 2015, *ApJ*, 812, 167. doi:10.1088/0004-637X/812/2/167
- Graham, M. J., Kulkarni, S. R., Bellm, E. C., et al. 2019, *PASP*, 131, 078001. doi:10.1088/1538-3873/ab006c
- Heber, U. 2023, arXiv:2304.02969. doi:10.48550/arXiv.2304.02969
- Hermes, J. J., Brown, W. R., Kilic, M., et al. 2014, *ApJ*, 792, 39. doi:10.1088/0004-637X/792/1/39
- Irrgang, A., Geier, S., Heber, U., et al. 2021, *A&A*, 650, A102. doi:10.1051/0004-6361/202038757

⁸ <http://www.hpcc.ttu.edu>

⁹ <http://www.astropy.org>

- Irrgang, A., Przybilla, N., & Meynet, G. 2022, *Nature Astronomy*, 6, 1414. doi:10.1038/s41550-022-01809-6
- Istrate, A. G., Marchant, P., Tauris, T. M., et al. 2016, *A&A*, 595, A35. doi:10.1051/0004-6361/201628874
- Ivezić, Ž., Kahn, S. M., Tyson, J. A., et al. 2019, *ApJ*, 873, 111. doi:10.3847/1538-4357/ab042c
- Kenyon, S. J. & Garcia, M. R. 1986, *AJ*, 91, 125. doi:10.1086/113991
- Kilic, M., Stanek, K. Z., & Pinsonneault, M. H. 2007, *ApJ*, 671, 761. doi:10.1086/522228
- Kilic, M., Brown, W. R., Allende Prieto, C., et al. 2011, *ApJ*, 727, 3. doi:10.1088/0004-637X/727/1/3
- Kilic, M., Brown, W. R., Allende Prieto, C., et al. 2012, *ApJ*, 751, 141. doi:10.1088/0004-637X/751/2/141
- Kilic, M., Brown, W. R., Heinke, C. O., et al. 2016, *MNRAS*, 460, 4176. doi:10.1093/mnras/stw1277
- Kilic, M., Bédard, A., Bergeron, P., et al. 2020, *MNRAS*, 493, 2805. doi:10.1093/mnras/staa466
- Kilic, M., Moss, A. G., Kosakowski, A., et al. 2023, *MNRAS*, 518, 2341. doi:10.1093/mnras/stac3182
- Korol, V., Rossi, E. M., Groot, P. J., et al. 2017, *MNRAS*, 470, 1894. doi:10.1093/mnras/stx1285
- Kosakowski, A., Kilic, M., Brown, W. R., et al. 2020, *ApJ*, 894, 53. doi:10.3847/1538-4357/ab8300
- Kosakowski, Alekzander, Brown, Warren, Kilic, Mukremin, Kupfer, Thomas, Bédard, Antoine, Gianninas, Alex, Agüeros, Marcel, & Barrientos, Manuel. (2023). The ELM Survey South II [Data set]. Zenodo. <https://doi.org/10.5281/zenodo.7849976>
- Kovács, G., Zucker, S., & Mazeh, T. 2002, *A&A*, 391, 369. doi:10.1051/0004-6361:20020802
- Kupfer, T., Prince, T. A., van Roestel, J., et al. 2021, *MNRAS*, 505, 1254. doi:10.1093/mnras/stab1344
- Kupfer, T., Korol, V., Littenberg, T. B., et al. 2023, arXiv:2302.12719
- Kurtz, M. J. & Mink, D. J. 1998, *PASP*, 110, 934. doi:10.1086/316207
- Li, Z., Chen, X., Chen, H.-L., et al. 2019, *ApJ*, 871, 148. doi:10.3847/1538-4357/aaf9a1
- Li, Z., Chen, X., Chen, H.-L., et al. 2020, *ApJ*, 893, 2. doi:10.3847/1538-4357/ab7dc2
- Liebert, J., Bergeron, P., & Holberg, J. B. 2005, *ApJS*, 156, 47. doi:10.1086/425738
- Lomb, N. R. 1976, *Ap&SS*, 39, 447. doi:10.1007/BF00648343
- Mainzer, A., Bauer, J., Grav, T., et al. 2011, *ApJ*, 731, 53. doi:10.1088/0004-637X/731/1/53
- Martin, D. C., Fanson, J., Schiminovich, D., et al. 2005, *ApJL*, 619, L1. doi:10.1086/426387
- Masci, F. J., Laher, R. R., Rusholme, B., et al. 2019, *PASP*, 131, 018003. doi:10.1088/1538-3873/aae8ac
- Nelemans, G., Yungelson, L. R., & Portegies Zwart, S. F. 2001, *A&A*, 375, 890. doi:10.1051/0004-6361:20010683
- Onken, C. A., Wolf, C., Bessell, M. S., et al. 2019, *PASA*, 36, e033. doi:10.1017/pasa.2019.27
- Pelisoli, I. & Vos, J. 2019, *MNRAS*, 488, 2892. doi:10.1093/mnras/stz1876
- Przybilla, N., Nieva, M.-F., & Butler, K. 2011, *Journal of Physics Conference Series*, 328, 012015. doi:10.1088/1742-6596/328/1/012015
- Ricker, G. R., Winn, J. N., Vanderspek, R., et al. 2015, *Journal of Astronomical Telescopes, Instruments, and Systems*, 1, 014003. doi:10.1117/1.JATIS.1.1.014003
- Roelofs, G. H. A., Groot, P. J., Benedict, G. F., et al. 2007, *ApJ*, 666, 1174. doi:10.1086/520491
- Scargle, J. D. 1982, *ApJ*, 263, 835. doi:10.1086/160554
- Scherbak, P. & Fuller, J. 2023, *MNRAS*, 518, 3966. doi:10.1093/mnras/stac3313
- Schlafly, E. F. & Finkbeiner, D. P. 2011, *ApJ*, 737, 103. doi:10.1088/0004-637X/737/2/103
- Shanks, T., Metcalfe, N., Chehade, B., et al. 2015, *MNRAS*, 451, 4238. doi:10.1093/mnras/stv1130
- Shen, K. J. 2015, *ApJL*, 805, L6. doi:10.1088/2041-8205/805/1/L6
- Schönrich, R., Binney, J., & Dehnen, W. 2010, *MNRAS*, 403, 1829. doi:10.1111/j.1365-2966.2010.16253.x
- Skrutskie, M. F., Cutri, R. M., Stiening, R., et al. 2006, *AJ*, 131, 1163. doi:10.1086/498708
- Southworth, J., Maxted, P. F. L., & Smalley, B. 2004, *MNRAS*, 351, 1277. doi:10.1111/j.1365-2966.2004.07871.x
- Southworth, J. 2013, *A&A*, 557, A119. doi:10.1051/0004-6361/201322195
- Stassun, K. G., Oelkers, R. J., Pepper, J., et al. 2018, *AJ*, 156, 102. doi:10.3847/1538-3881/aad050
- Timpano, S. E., Rubbo, L. J., & Cornish, N. J. 2006, *PhRvD*, 73, 122001. doi:10.1103/PhysRevD.73.122001
- Tremblay, P.-E., Ludwig, H.-G., Steffen, M., et al. 2011, *A&A*, 531, L19. doi:10.1051/0004-6361/201117310
- Tremblay, P.-E., Gianninas, A., Kilic, M., et al. 2015, *ApJ*, 809, 148. doi:10.1088/0004-637X/809/2/148
- VanderPlas, J. T. 2018, *ApJS*, 236, 16. doi:10.3847/1538-4365/aab766
- Wang, K., Németh, P., Luo, Y., et al. 2022, *ApJ*, 936, 5. doi:10.3847/1538-4357/ac847c
- Wright, E. L., Eisenhardt, P. R. M., Mainzer, A. K., et al. 2010, *AJ*, 140, 1868. doi:10.1088/0004-6256/140/6/1868
- Zhang, X., Jeffery, C. S., Chen, X., et al. 2014, *MNRAS*, 445, 660. doi:10.1093/mnras/stu1741

Object	HJD (−2450000 days)	v_r (km s ^{−1})
J0135+2359	9192.787768	133.7 ± 7.0
J0135+2359	9548.737532	7.4 ± 10.6
J0135+2359	9548.786808	−17.7 ± 10.0
J0135+2359	9548.834528	−72.6 ± 9.5
J0135+2359	9549.572076	110.4 ± 16.5
J0135+2359	9549.712261	117.2 ± 13.1
J0135+2359	9549.776407	139.2 ± 9.6
J0135+2359	9549.821702	74.6 ± 12.7
J0135+2359	9549.827105	98.2 ± 13.5
J0135+2359	9549.831960	84.5 ± 14.8
J0135+2359	9549.837437	103.3 ± 14.2
J0135+2359	9550.562962	−14.0 ± 8.6
J0135+2359	9550.782942	113.2 ± 8.5
J0135+2359	9551.560708	−192.1 ± 10.9
J0135+2359	9551.568185	−200.6 ± 13.3
J0135+2359	9551.574674	−171.2 ± 8.7
J0135+2359	9551.664734	−107.1 ± 8.3
J0135+2359	9551.767718	−1.4 ± 9.1
J0155−4148	8778.528269	120.9 ± 4.5
J0155−4148	8778.747847	93.1 ± 5.5
J0155−4148	8780.584034	107.9 ± 9.8
J0155−4148	8780.591087	62.2 ± 8.2
J0155−4148	8781.538707	199.1 ± 2.5
J0155−4148	8781.631074	103.9 ± 2.0
...

Table 4. Radial velocity measurements for the 28 new binaries identified in this work. This table has been truncated. The complete version of this table is available in the supplemental data files.

8. APPENDIX

Table 5. Atmospheric parameters (assuming pure-hydrogen atmospheres) for objects observed as part of our follow-up campaign with $\log g > 5.0$. Objects which show periodic photometric variability in ZTF DR16 or TESS high-cadence data, and objects which were classified as ELM white dwarf candidates in Pelisoli & Vos (2019), are marked. Optical spectroscopy for each object presented in this table is available in a public Zenodo archive (Kosakowski et al. 2023).

SOURCE_ID (Gaia DR3)	R.A. (2016.0)	Decl. (2016.0)	T_{eff} (K)	$\log g$ (cm s $^{-2}$)	Gaia G (mag)	Gaia $(BP - RP)$ (mag)	Gaia Parallax (mas)
2882002220454588672	00:03:06.730	+40:39:27.119	19250 ± 470	8.00 ± 0.07	18.49	0.01 ± 0.01	1.71 ± 0.32
2739093475807603584	00:03:19.659	+02:26:23.089	21790 ± 1190	8.35 ± 0.18	16.39	-0.098 ± 0.005	6.32 ± 0.07
2798386113507604992 ^c	00:03:33.944	+20:16:26.238	17760 ± 540	7.72 ± 0.10	18.95	0.07 ± 0.02	2.25 ± 0.25
2874194833198918400	00:03:42.161	+32:44:15.731	16410 ± 440	7.79 ± 0.08	18.22	0.22 ± 0.01	3.30 ± 0.14
2448821478361661696	00:05:04.760	-01:27:08.384	31340 ± 1380	7.68 ± 0.31	16.63	-0.33 ± 0.01	3.66 ± 0.07
420251387300980096 ^c	00:07:09.001	+53:49:47.474	32980 ± 1930	6.15 ± 0.35	16.17	0.071 ± 0.004	0.96 ± 0.04
2859826106009305216 ^c	00:12:32.540	+27:47:09.460	25990 ± 860	7.37 ± 0.13	16.98	-0.31 ± 0.01	2.89 ± 0.09
2768409887481718272 ^c	00:12:45.662	+14:39:56.678	14580 ± 410	7.38 ± 0.08	18.19	0.07 ± 0.01	2.78 ± 0.18
2800210546895703680 ^c	00:15:48.404	+21:27:46.332	32970 ± 1020	7.35 ± 0.21	17.51	-0.30 ± 0.01	1.85 ± 0.10
2876543282660374784	00:17:44.512	+35:58:26.087	18410 ± 430	7.95 ± 0.07	18.85	0.03 ± 0.02	1.88 ± 0.23
2863621134816230528 ^{ac}	00:18:11.384	+33:11:08.826	30630 ± 590	7.44 ± 0.09	18.04	-0.29 ± 0.01	1.28 ± 0.14
2855799415254881408	00:20:22.382	+26:40:10.956	11820 ± 220	8.02 ± 0.13	16.11	-0.111 ± 0.005	10.51 ± 0.05
380560941677424768 ^b	00:33:52.632	+38:55:29.608	34130 ± 700	7.30 ± 0.13	18.34	-0.19 ± 0.02	1.19 ± 0.17
4907063048361514496	00:40:00.768	-58:40:31.721	38240 ± 750	7.28 ± 0.09	17.58	-0.24 ± 0.02	1.14 ± 0.08
2542961560852591744	00:40:22.906	-00:21:30.172	16470 ± 510	8.16 ± 0.09	14.85	0.046 ± 0.004	18.24 ± 0.03
2550740120286280576	00:45:36.928	+02:40:14.491	15140 ± 480	5.03 ± 0.10	18.85	0.31 ± 0.02	0.93 ± 0.27
2809085018776598528 ^c	00:49:11.206	+28:16:02.255	27850 ± 2870	5.68 ± 0.42	16.56	-0.32 ± 0.01	0.59 ± 0.07
377520826387065856	00:52:04.391	+45:05:33.799	11730 ± 180	8.21 ± 0.11	16.01	-0.039 ± 0.004	13.28 ± 0.04
2776836514532338304 ^c	00:52:44.411	+13:16:35.972	36500 ± 1560	7.33 ± 0.28	17.94	-0.32 ± 0.01	1.11 ± 0.13
374447996328984704 ^c	01:01:10.344	+41:06:04.921	21740 ± 510	7.36 ± 0.07	18.41	-0.24 ± 0.02	1.68 ± 0.17
2785461702216001152	01:07:25.996	+19:09:32.166	21940 ± 1260	7.56 ± 0.19	15.64	-0.276 ± 0.005	5.93 ± 0.05
2579742694406440064 ^c	01:09:29.505	+09:19:51.845	32350 ± 1030	7.81 ± 0.23	17.37	-0.36 ± 0.01	1.53 ± 0.11
2534408386884529920	01:12:58.398	-00:59:52.519	19380 ± 610	7.58 ± 0.10	18.84	-0.27 ± 0.03	1.09 ± 0.25
373358998783703808	01:16:00.832	+42:49:38.323	12970 ± 200	5.06 ± 0.05	18.71	-0.00 ± 0.02	0.57 ± 0.18
320040145192523264 ^c	01:16:20.951	+33:41:16.094	13880 ± 240	7.42 ± 0.05	18.16	-0.06 ± 0.01	2.16 ± 0.16
2482810406432480512 ^b	01:16:51.573	-04:40:47.107	45500 ± 870	7.58 ± 0.10	18.34	-0.25 ± 0.02	1.02 ± 0.18
2471069512033475712	01:21:49.346	-10:08:00.751	17340 ± 490	7.95 ± 0.09	17.31	0.07 ± 0.01	8.58 ± 0.10
2563353721975582464 ^c	01:25:43.673	+04:55:14.686	18120 ± 450	7.60 ± 0.08	18.15	0.19 ± 0.01	4.07 ± 0.19
531617690261698304 ^{ab}	01:33:38.050	+68:03:32.789	34860 ± 1030	7.58 ± 0.21	16.72	0.21 ± 0.01	2.60 ± 0.05
296853330452496000	01:34:46.322	+28:26:16.202	12300 ± 330	7.89 ± 0.11	16.91	0.02 ± 0.01	5.68 ± 0.07
315437516503244928	01:35:01.880	+31:17:10.212	18700 ± 500	7.93 ± 0.09	19.07	-0.17 ± 0.02	2.33 ± 0.32
322765211746880384	01:38:52.560	+38:34:01.819	34230 ± 680	7.83 ± 0.12	18.46	-0.36 ± 0.02	1.29 ± 0.18
347329027362621056	01:40:12.938	+41:29:27.074	25380 ± 550	7.76 ± 0.08	18.36	-0.28 ± 0.01	2.13 ± 0.20
319243613441880320	01:43:20.592	+36:28:42.978	36240 ± 1140	8.27 ± 0.21	17.23	-0.37 ± 0.01	2.39 ± 0.09
5139287360210678144 ^c	01:48:11.827	-19:48:14.188	15090 ± 240	7.74 ± 0.05	18.82	0.03 ± 0.01	1.56 ± 0.19

Table 5 *continued*

Table 5 (*continued*)

SOURCE_ID (Gaia DR3)	R.A. (2016.0)	Decl. (2016.0)	T_{eff} (K)	$\log g$ (cm s $^{-2}$)	Gaia G (mag)	Gaia $(BP - RP)$ (mag)	Gaia Parallax (mas)
92185017673400960	01:52:27.290	+18:20:14.374	34580 ± 990	7.81 ± 0.20	17.43	-0.19 ± 0.01	1.99 ± 0.12
5134761186235143424	01:55:58.754	-22:38:22.520	23910 ± 610	7.58 ± 0.09	17.64	-0.32 ± 0.01	2.30 ± 0.10
2466766946939761280 ^b	01:58:41.010	-06:28:41.650	22740 ± 550	7.74 ± 0.08	16.91	0.12 ± 0.01	3.55 ± 0.08
4968866493879269760 ^c	01:59:48.100	-35:16:51.229	21850 ± 720	7.52 ± 0.10	17.92	-0.24 ± 0.01	1.97 ± 0.10
104648944047154432	02:08:47.713	+25:14:08.045	20880 ± 440	8.05 ± 0.06	13.23	-0.208 ± 0.004	25.59 ± 0.03
5136945744040876928	02:09:30.476	-20:19:33.535	27690 ± 500	7.53 ± 0.07	18.30	-0.29 ± 0.02	1.68 ± 0.17
4715247167518325376	02:10:35.380	-57:49:57.976	26780 ± 460	7.58 ± 0.06	17.66	-0.33 ± 0.01	2.29 ± 0.07
331359166428843904	02:13:28.349	+37:16:49.814	24300 ± 2040	6.79 ± 0.28	17.80	-0.29 ± 0.01	1.92 ± 0.14
4744277057630500352	02:13:54.959	-53:04:53.962	26430 ± 400	7.42 ± 0.05	17.29	-0.33 ± 0.01	2.34 ± 0.07
2493466422156808576	02:23:17.915	-02:42:52.495	28000 ± 670	7.36 ± 0.10	18.11	-0.05 ± 0.02	1.36 ± 0.16
5131327656235273088 ^c	02:27:41.362	-18:59:25.656	17550 ± 2300	7.81 ± 0.45	15.98	-0.120 ± 0.004	6.45 ± 0.04
76220791737582720	02:28:45.867	+15:42:02.599	37170 ± 1120	7.21 ± 0.19	18.26	-0.07 ± 0.02	1.20 ± 0.19
131694078232129792	02:30:14.426	+30:56:11.627	24620 ± 550	7.30 ± 0.07	18.55	-0.08 ± 0.02	1.63 ± 0.19
5130174745278506112	02:33:01.035	-20:25:59.635	16810 ± 590	7.55 ± 0.12	19.63	-0.14 ± 0.04	1.88 ± 0.32
18117653818752512	02:35:47.678	+05:35:24.083	24640 ± 760	7.31 ± 0.11	15.79	-0.36 ± 0.01	5.22 ± 0.07
4741227287252719872	02:38:43.420	-55:01:27.966	18700 ± 410	7.41 ± 0.07	17.43	-0.22 ± 0.01	2.22 ± 0.06
2502595323604529408	02:40:09.470	+01:51:49.248	17710 ± 300	7.41 ± 0.05	18.44	-0.19 ± 0.02	1.92 ± 0.18
4952731126381731328	02:45:09.857	-38:05:40.247	14240 ± 280	7.84 ± 0.05	18.06	-0.09 ± 0.01	2.42 ± 0.10
6306661258129280	02:48:45.909	+05:39:21.758	12410 ± 280	7.86 ± 0.09	19.04	0.13 ± 0.02	1.50 ± 0.38
115708721056790144 ^c	03:01:45.948	+26:55:44.879	30780 ± 810	7.76 ± 0.16	18.55	-0.08 ± 0.02	1.43 ± 0.19
5104166386135159936	03:06:39.346	-19:02:24.893	35530 ± 650	8.20 ± 0.09	17.32	-0.08 ± 0.01	2.71 ± 0.08
3262674487682440448 ^c	03:18:13.332	-01:07:11.806	12450 ± 1480	7.52 ± 0.44	14.71	-0.062 ± 0.004	14.25 ± 0.03
3260723782255411456	03:23:22.673	-03:54:20.808	28440 ± 630	7.88 ± 0.10	18.50	-0.32 ± 0.03	2.22 ± 0.24
237133566847520000 ^c	03:38:47.068	+41:34:24.100	23460 ± 430	5.82 ± 0.06	15.09	-0.061 ± 0.004	1.65 ± 0.03
69886853143994496 ^c	03:44:22.259	+25:14:53.293	28280 ± 1340	6.45 ± 0.22	15.55	-0.006 ± 0.004	1.79 ± 0.04
5113854281871286912	03:45:32.977	-14:04:58.102	11140 ± 320	5.02 ± 0.10	18.64	0.18 ± 0.02	0.58 ± 0.18
4858747758657659136	03:51:23.934	-34:45:50.306	15450 ± 450	7.34 ± 0.09	18.14	-0.18 ± 0.01	2.54 ± 0.10
4887600528615197184	03:52:10.364	-30:25:23.981	28540 ± 890	7.40 ± 0.15	17.21	-0.21 ± 0.01	2.45 ± 0.07
3251978198050225664	04:03:24.704	-03:28:51.614	26600 ± 450	7.43 ± 0.06	16.68	-0.30 ± 0.01	3.32 ± 0.06
4844023064578952320 ^c	04:04:44.429	-39:50:43.206	35120 ± 780	7.54 ± 0.13	17.66	-0.27 ± 0.02	1.58 ± 0.07
4681729620697295360 ^a	04:10:33.371	-58:52:03.482	32040 ± 480	7.28 ± 0.06	17.57	-0.15 ± 0.02	1.52 ± 0.07
4830937162517646592	04:13:45.134	-47:37:25.612	18500 ± 360	7.84 ± 0.06	16.54	-0.14 ± 0.01	5.33 ± 0.04
166283580171410816	04:20:32.033	+31:09:08.701	34450 ± 760	7.25 ± 0.13	18.70	0.05 ± 0.02	1.44 ± 0.20
3204352783173513728 ^b	04:31:03.755	-04:17:02.555	36010 ± 700	7.59 ± 0.11	17.92	-0.32 ± 0.02	0.98 ± 0.14
3185254609798003328 ^c	04:34:38.049	-10:14:07.246	17460 ± 2920	8.03 ± 0.63	16.53	0.004 ± 0.004	6.68 ± 0.05
3229440649222191616	04:36:59.954	-01:15:53.903	31190 ± 550	8.05 ± 0.08	17.91	-0.30 ± 0.01	2.68 ± 0.12
4814354976686021888	04:47:19.788	-44:44:10.622	20900 ± 530	7.69 ± 0.08	16.93	-0.27 ± 0.01	3.71 ± 0.05
3225359193340812288 ^c	04:59:20.296	-02:28:06.650	32550 ± 1450	6.09 ± 0.29	15.05	-0.398 ± 0.004	1.11 ± 0.04
2979874526445650560	05:01:59.217	-17:09:56.642	26160 ± 410	7.48 ± 0.05	18.42	-0.12 ± 0.01	1.30 ± 0.14
3211273483020379136	05:07:42.284	-05:50:52.811	31150 ± 540	7.82 ± 0.08	18.31	-0.35 ± 0.01	1.50 ± 0.17

Table 5 *continued*

Table 5 (*continued*)

SOURCE_ID (Gaia DR3)	R.A. (2016.0)	Decl. (2016.0)	T_{eff} (K)	$\log g$ (cm s $^{-2}$)	Gaia G (mag)	Gaia $(BP - RP)$ (mag)	Gaia Parallax (mas)
2971802603565750016	05:31:27.482	-15:56:26.520	29490 ± 470	7.95 ± 0.06	16.55	-0.325 ± 0.005	3.97 ± 0.06
4821683294701731456 ^c	05:32:25.215	-36:40:57.058	24710 ± 640	7.30 ± 0.09	17.38	-0.30 ± 0.01	2.28 ± 0.06
2965034525384116864	05:32:46.106	-21:03:40.381	27600 ± 460	7.53 ± 0.06	17.72	-0.22 ± 0.01	1.82 ± 0.09
3402486457838073728	05:38:02.721	+19:53:02.893	37120 ± 1080	7.33 ± 0.16	18.80	0.02 ± 0.02	0.96 ± 0.29
480570075502703488 ^c	05:39:59.130	+66:30:43.434	39310 ± 2520	7.13 ± 0.27	16.43	-0.228 ± 0.005	1.61 ± 0.05
191727718051389312 ^c	05:47:06.231	+40:08:22.524	28290 ± 4040	5.33 ± 0.53	15.75	-0.061 ± 0.004	1.02 ± 0.05
4805297955811200384 ^c	05:47:14.337	-39:22:53.227	31790 ± 520	7.59 ± 0.07	18.26	-0.17 ± 0.01	1.25 ± 0.11
2904788774305591168	05:49:05.586	-27:51:03.064	21370 ± 620	7.44 ± 0.09	19.18	-0.16 ± 0.02	1.34 ± 0.18
3123004865638910208 ^c	06:09:30.047	+01:00:43.243	35800 ± 2690	6.20 ± 0.45	16.36	-0.067 ± 0.005	0.71 ± 0.06
1106926566694585984	06:19:13.539	+69:11:37.003	36910 ± 750	7.98 ± 0.10	16.89	-0.092 ± 0.005	3.22 ± 0.06
2999745209821746176 ^c	06:20:42.669	-13:07:30.864	36350 ± 3360	6.15 ± 0.53	16.14	-0.170 ± 0.005	1.10 ± 0.05
943429565599232128 ^c	06:34:49.904	+38:03:51.977	22560 ± 430	7.18 ± 0.06	17.13	-0.19 ± 0.01	2.31 ± 0.08
967722411725539456 ^c	06:38:40.371	+48:29:50.784	30210 ± 5070	5.43 ± 0.82	16.15	-0.309 ± 0.005	0.68 ± 0.06
1141248917368171648 ^c	06:43:34.284	+79:20:36.190	16930 ± 530	7.91 ± 0.10	18.86	-0.18 ± 0.05	2.24 ± 0.16
3351216303643796096 ^c	06:45:32.028	+11:40:03.173	27350 ± 3840	5.30 ± 0.48	16.85	0.07 ± 0.01	0.67 ± 0.06
3352835983053282304 ^c	06:47:34.863	+13:50:11.332	31730 ± 1640	6.16 ± 0.33	16.80	-0.19 ± 0.01	0.55 ± 0.07
1106390211177861888 ^c	06:47:46.546	+69:15:34.430	32030 ± 680	7.27 ± 0.12	17.90	-0.46 ± 0.01	1.47 ± 0.11
1000497070938042496 ^c	06:58:37.717	+57:12:35.755	34520 ± 1960	5.25 ± 0.28	16.21	-0.367 ± 0.005	0.56 ± 0.06
979204650309974016	07:00:04.137	+49:43:38.687	35320 ± 1580	7.60 ± 0.33	17.43	-0.31 ± 0.01	2.44 ± 0.11
990086409514581760	07:07:17.295	+58:01:36.512	23590 ± 510	7.42 ± 0.07	16.92	-0.30 ± 0.01	3.31 ± 0.07
5490015871367837440 ^c	07:07:30.007	-56:17:43.206	32240 ± 480	7.14 ± 0.06	15.89	-0.343 ± 0.004	2.34 ± 0.03
3161169390978526592 ^c	07:12:06.982	+13:23:49.200	14790 ± 490	7.85 ± 0.08	18.83	-0.15 ± 0.02	2.00 ± 0.23
1102031472205224832 ^b	07:14:52.278	+66:29:28.648	22320 ± 760	7.47 ± 0.11	18.87	0.26 ± 0.01	1.39 ± 0.17
989858913686629248	07:20:10.814	+57:30:54.979	30920 ± 1030	7.58 ± 0.21	17.87	-0.34 ± 0.01	2.17 ± 0.13
900688761191934208	07:30:30.416	+41:15:39.827	29150 ± 800	7.96 ± 0.14	17.64	-0.40 ± 0.01	2.66 ± 0.12
3169165486210495488 ^c	07:34:29.881	+16:48:22.968	16540 ± 560	8.02 ± 0.10	19.02	0.04 ± 0.04	2.04 ± 0.30
3165507445385638528	07:42:11.606	+14:53:17.970	17080 ± 510	7.74 ± 0.09	19.02	-0.01 ± 0.03	2.32 ± 0.24
671699491725392128 ^c	07:45:44.371	+18:58:49.631	15620 ± 400	7.69 ± 0.08	17.54	0.07 ± 0.01	3.93 ± 0.10
668912126670207360 ^c	08:02:42.951	+17:50:00.848	21930 ± 1520	7.66 ± 0.23	16.27	-0.216 ± 0.005	4.23 ± 0.06
3063885736023355904 ^c	08:06:50.022	-07:16:36.109	13640 ± 550	6.46 ± 0.14	18.55	-0.07 ± 0.02	0.93 ± 0.18
653228761532233216 ^c	08:07:39.280	+13:21:11.434	15560 ± 1910	7.44 ± 0.43	16.43	0.097 ± 0.004	8.71 ± 0.05
3096525945581800576 ^b	08:11:26.652	+05:39:11.441	26860 ± 720	7.87 ± 0.11	16.54	0.02 ± 0.01	4.57 ± 0.06
3070115057805517568 ^c	08:18:41.061	-02:14:13.434	33450 ± 1740	5.13 ± 0.33	16.49	-0.35 ± 0.01	0.50 ± 0.06
3090361426264736000 ^c	08:20:00.642	+02:23:27.107	14760 ± 370	7.53 ± 0.07	18.44	-0.01 ± 0.02	2.29 ± 0.19
928585329693880832 ^c	08:20:10.339	+45:43:01.704	17360 ± 250	7.46 ± 0.04	18.21	-0.08 ± 0.01	2.38 ± 0.18
3090457599171887104	08:21:01.664	+02:32:09.316	23240 ± 950	7.54 ± 0.14	18.81	0.35 ± 0.02	1.40 ± 0.22
1123423639154702464 ^c	08:21:42.669	+73:55:29.406	35660 ± 1370	6.06 ± 0.24	14.43	-0.452 ± 0.004	1.75 ± 0.04
709064710767864064 ^c	08:23:59.152	+31:11:51.893	19680 ± 390	7.57 ± 0.06	18.29	-0.20 ± 0.01	1.98 ± 0.18
5196549827003398656	08:28:48.624	-80:19:35.026	24480 ± 370	7.54 ± 0.05	15.33	-0.328 ± 0.004	7.14 ± 0.03
707909910025230080	08:28:55.281	+29:21:00.310	15560 ± 390	7.74 ± 0.07	18.85	-0.00 ± 0.03	1.95 ± 0.23

Table 5 *continued*

Table 5 (*continued*)

SOURCE_ID (Gaia DR3)	R.A. (2016.0)	Decl. (2016.0)	T_{eff} (K)	$\log g$ (cm s $^{-2}$)	Gaia G (mag)	Gaia $(BP - RP)$ (mag)	Gaia Parallax (mas)
3073641569552516864 ^c	08:36:01.849	-00:44:22.974	26820 \pm 480	6.02 \pm 0.06	15.92	-0.349 \pm 0.004	1.06 \pm 0.06
662771594747150976	08:36:12.031	+19:17:55.853	33230 \pm 2400	5.36 \pm 0.48	15.69	-0.092 \pm 0.005	0.53 \pm 0.07
664631178147534720 ^c	08:36:19.698	+20:57:47.358	30820 \pm 1540	6.03 \pm 0.29	16.31	-0.43 \pm 0.01	0.54 \pm 0.09
3078353045597053696 ^c	08:40:14.857	+00:42:39.028	33580 \pm 1900	5.92 \pm 0.37	16.47	-0.325 \pm 0.005	0.59 \pm 0.05
582675157663938304	08:48:23.744	+05:08:44.930	16100 \pm 330	7.78 \pm 0.07	17.42	-0.12 \pm 0.01	2.59 \pm 0.09
605052074715179008 ^c	08:54:08.733	+12:22:26.504	15020 \pm 280	7.50 \pm 0.05	18.50	-0.02 \pm 0.01	2.41 \pm 0.20
684882528766947456	08:57:45.557	+20:38:50.381	11400 \pm 310	5.04 \pm 0.10	18.20	0.22 \pm 0.01	0.90 \pm 0.18
718805520500404608	09:00:14.503	+37:57:49.241	22340 \pm 540	7.48 \pm 0.08	19.15	-0.38 \pm 0.03	0.95 \pm 0.27
611215077906912640 ^c	09:03:00.839	+17:21:32.170	11690 \pm 210	7.83 \pm 0.06	18.38	0.01 \pm 0.01	2.50 \pm 0.18
1009623532844468480	09:08:46.276	+45:16:52.561	11870 \pm 330	7.87 \pm 0.10	18.27	-0.09 \pm 0.01	2.94 \pm 0.16
1009618997359086848	09:09:19.116	+45:10:51.697	16700 \pm 460	8.00 \pm 0.08	19.04	-0.04 \pm 0.02	2.14 \pm 0.30
638506468336791296	09:17:29.690	+21:43:33.452	20540 \pm 540	7.85 \pm 0.08	18.85	-0.02 \pm 0.02	1.51 \pm 0.29
3845945232756311936 ^{ac}	09:23:37.323	+03:53:09.208	31520 \pm 730	7.35 \pm 0.14	17.53	-0.35 \pm 0.01	1.61 \pm 0.12
817452604232788224	09:24:39.388	+42:36:33.415	11260 \pm 260	7.87 \pm 0.08	18.79	-0.15 \pm 0.02	1.41 \pm 0.18
5689579636989620608 ^c	09:25:09.586	-14:11:22.556	26680 \pm 3340	7.07 \pm 0.48	15.39	-0.374 \pm 0.004	4.07 \pm 0.04
1063375422215251456	09:36:36.353	+62:56:05.593	15550 \pm 580	7.54 \pm 0.12	18.24	0.55 \pm 0.01	2.54 \pm 0.12
794276587043539456 ^c	09:37:08.551	+33:34:04.141	24620 \pm 830	7.33 \pm 0.12	16.36	-0.323 \pm 0.005	3.11 \pm 0.08
616823209979081472 ^b	09:52:50.473	+15:53:04.013	22810 \pm 620	7.58 \pm 0.09	18.31	0.42 \pm 0.02	1.35 \pm 0.20
3879591353717543040	09:53:02.996	+10:32:20.094	11610 \pm 240	7.81 \pm 0.07	18.79	-0.13 \pm 0.02	1.73 \pm 0.25
1146182357322101120	10:07:52.208	+81:40:46.549	19280 \pm 740	7.66 \pm 0.13	18.63	0.30 \pm 0.01	1.41 \pm 0.21
3752200596493839232 ^c	10:24:32.206	-14:34:20.503	9290 \pm 150	8.20 \pm 0.10	16.81	-0.13 \pm 0.01	2.82 \pm 0.09
3767870664414250112 ^b	10:26:53.472	-10:13:30.194	22150 \pm 670	7.53 \pm 0.09	18.35	-0.15 \pm 0.03	1.65 \pm 0.19
5467851842959399808 ^{ab}	10:30:39.621	-27:54:38.876	32020 \pm 800	7.75 \pm 0.16	18.31	-0.04 \pm 0.02	1.31 \pm 0.18
1048058916002814080	10:33:50.070	+60:44:01.421	19570 \pm 530	7.50 \pm 0.09	18.54	-0.24 \pm 0.01	1.86 \pm 0.14
5468388683808323328	10:35:51.946	-26:43:01.996	23340 \pm 810	7.48 \pm 0.12	18.92	-0.27 \pm 0.02	1.37 \pm 0.24
1071978142925329280	10:36:05.668	+67:38:17.232	9370 \pm 160	8.37 \pm 0.16	17.67	-0.26 \pm 0.01	2.22 \pm 0.08
3754558774057309568	10:36:42.062	-11:47:42.065	23940 \pm 590	7.86 \pm 0.09	19.56	-0.25 \pm 0.04	1.26 \pm 0.37
3777010874511580800 ^c	10:51:15.599	-04:54:52.938	21230 \pm 610	7.39 \pm 0.09	17.92	-0.21 \pm 0.01	2.14 \pm 0.16
3801572246288990720	10:51:59.289	-02:48:05.868	27700 \pm 460	7.29 \pm 0.06	17.49	-0.34 \pm 0.01	1.26 \pm 0.20
3865904461176307840 ^c	10:52:13.140	+08:06:31.482	14480 \pm 660	7.50 \pm 0.15	17.73	0.06 \pm 0.01	3.31 \pm 0.13
3758426443647179008	11:06:21.270	-10:56:47.407	15870 \pm 420	7.70 \pm 0.09	18.17	-0.11 \pm 0.01	1.98 \pm 0.16
3803538104360099328	11:06:27.670	-01:05:14.698	30280 \pm 630	7.56 \pm 0.11	16.47	0.06 \pm 0.01	3.03 \pm 0.08
3783864852042143616	11:22:56.309	-06:45:05.792	25160 \pm 1180	7.25 \pm 0.18	17.97	0.15 \pm 0.01	1.77 \pm 0.13
3812632092018399104 ^c	11:24:21.658	+03:30:26.003	20360 \pm 500	7.65 \pm 0.07	18.16	-0.23 \pm 0.02	2.02 \pm 0.16
3796545519645331584	11:27:21.271	-02:08:37.464	23520 \pm 720	7.90 \pm 0.10	16.39	-0.260 \pm 0.005	5.39 \pm 0.07
3484922002822079872 ^c	11:35:24.140	-26:54:41.544	18160 \pm 350	7.52 \pm 0.06	17.62	-0.12 \pm 0.01	2.91 \pm 0.11
3895861965440903680 ^c	11:51:24.105	+03:41:47.263	19950 \pm 470	7.61 \pm 0.07	18.13	-0.24 \pm 0.01	2.14 \pm 0.14
3892319850076956032 ^c	11:53:16.969	+01:45:08.284	15000 \pm 620	7.46 \pm 0.11	18.74	0.01 \pm 0.01	2.15 \pm 0.26
4013124296427540096	12:08:34.821	+29:08:50.208	15980 \pm 430	7.82 \pm 0.07	18.89	-0.19 \pm 0.02	2.06 \pm 0.30
3501205731372521984	12:35:49.147	-23:28:06.280	19410 \pm 610	7.73 \pm 0.11	18.98	-0.02 \pm 0.02	1.43 \pm 0.24

Table 5 *continued*

Table 5 (*continued*)

SOURCE_ID (Gaia DR3)	R.A. (2016.0)	Decl. (2016.0)	T_{eff} (K)	$\log g$ (cm s $^{-2}$)	Gaia G (mag)	Gaia $(BP - RP)$ (mag)	Gaia Parallax (mas)
6157479215371911040	12:38:33.842	-35:07:23.412	16130 ± 320	7.45 ± 0.06	19.00	-0.09 ± 0.02	1.30 ± 0.22
3676893915531705984	12:47:29.573	-05:39:23.036	25440 ± 530	7.69 ± 0.07	18.44	-0.26 ± 0.02	1.31 ± 0.19
3525671553013347968 ^c	12:51:41.084	-13:50:12.520	15440 ± 390	7.54 ± 0.08	18.52	0.16 ± 0.02	2.62 ± 0.22
3625674673885031680 ^c	12:59:29.143	-10:17:48.257	16820 ± 410	7.58 ± 0.08	18.14	0.12 ± 0.01	2.90 ± 0.16
6193688224923108480	13:13:23.141	-25:03:08.309	28540 ± 440	7.44 ± 0.05	18.58	-0.25 ± 0.02	1.28 ± 0.19
1446939125851716864	13:16:26.562	+24:24:50.440	22670 ± 1380	7.28 ± 0.20	17.94	-0.32 ± 0.01	2.05 ± 0.13
3636151129911425408	13:19:09.855	-04:13:14.275	16100 ± 510	7.68 ± 0.09	17.41	-0.01 ± 0.01	2.42 ± 0.29
1718367456798754176	13:21:30.497	+79:58:32.311	27590 ± 700	8.00 ± 0.12	18.52	-0.09 ± 0.02	1.93 ± 0.18
3631612758228909696	13:29:04.203	-06:54:00.000	15980 ± 460	8.22 ± 0.09	19.58	-0.19 ± 0.03	1.85 ± 0.38
3741493212960873472	13:34:28.970	+14:06:47.412	16200 ± 690	7.80 ± 0.16	18.88	-0.15 ± 0.02	1.59 ± 0.23
6293400838501106432	13:45:45.625	-18:16:46.675	18630 ± 490	7.49 ± 0.08	19.22	-0.07 ± 0.03	1.42 ± 0.28
3725586917543559936	13:46:08.455	+10:27:09.882	20280 ± 880	7.69 ± 0.16	19.12	-0.11 ± 0.02	1.27 ± 0.28
3728966476985207936 ^c	13:51:53.790	+14:09:45.299	18690 ± 1110	8.16 ± 0.21	15.25	-0.190 ± 0.004	8.64 ± 0.03
6121727078670155648	14:02:16.856	-35:26:26.632	21500 ± 590	7.51 ± 0.08	19.22	0.24 ± 0.04	1.35 ± 0.38
6302470194522928384 ^c	14:04:55.459	-13:01:43.558	16030 ± 370	8.01 ± 0.07	18.54	-0.11 ± 0.02	2.07 ± 0.21
3640987851498162048	14:12:32.008	-05:49:43.979	14050 ± 620	7.45 ± 0.10	18.37	-0.10 ± 0.02	1.81 ± 0.19
6216651490910555008 ^c	14:32:14.140	-31:32:06.803	35310 ± 810	7.35 ± 0.14	18.18	-0.08 ± 0.02	1.31 ± 0.17
1603554764703627520 ^c	14:36:33.304	+50:10:26.843	17010 ± 270	6.68 ± 0.05	18.42	-0.19 ± 0.01	1.05 ± 0.13
6323667889648971520	14:45:12.622	-12:34:24.856	38300 ± 1940	7.62 ± 0.28	16.83	-0.34 ± 0.01	3.40 ± 0.10
6338539467313753856 ^b	14:45:32.863	-04:05:32.788	19990 ± 800	7.61 ± 0.14	18.39	-0.09 ± 0.01	2.06 ± 0.26
1185747286815299584	14:46:06.934	+14:24:20.959	16700 ± 480	7.56 ± 0.08	18.91	-0.01 ± 0.02	1.69 ± 0.24
1171774040214623744 ^c	14:46:16.111	+07:35:53.934	11180 ± 300	7.82 ± 0.15	18.43	-0.20 ± 0.02	1.84 ± 0.21
6202134673248731648	14:55:21.274	-36:09:18.914	13220 ± 380	5.51 ± 0.10	17.94	-0.05 ± 0.01	0.88 ± 0.14
1587468291113937152 ^c	14:58:00.877	+47:15:50.616	15800 ± 530	7.56 ± 0.11	18.86	0.04 ± 0.02	2.04 ± 0.17
6320134639096976512	15:07:12.554	-09:11:09.085	17930 ± 440	7.55 ± 0.08	18.62	-0.04 ± 0.02	1.75 ± 0.20
6334550507847433856	15:12:45.575	-05:57:16.974	25180 ± 900	7.55 ± 0.15	18.46	-0.15 ± 0.02	2.05 ± 0.19
1290428254138905216	15:13:50.075	+33:44:26.059	15070 ± 470	7.69 ± 0.09	17.29	-0.12 ± 0.01	3.68 ± 0.06
6209808611575247104	15:29:55.238	-29:22:11.068	30980 ± 1040	7.47 ± 0.21	18.44	0.07 ± 0.01	1.67 ± 0.20
1272514216129754496	15:36:41.442	+28:43:49.188	22580 ± 690	7.59 ± 0.10	18.38	-0.26 ± 0.01	1.89 ± 0.13
1190410040751247488	15:38:46.021	+12:07:47.874	13170 ± 430	7.88 ± 0.08	18.53	0.03 ± 0.02	2.34 ± 0.21
1209860985561813248	15:39:09.221	+18:48:17.863	12610 ± 320	5.18 ± 0.08	17.96	0.22 ± 0.01	1.24 ± 0.33
6260329800780772608 ^{b,c}	15:44:25.902	-18:16:51.305	35190 ± 820	7.13 ± 0.15	17.52	-0.20 ± 0.02	1.00 ± 0.11
1646202037605812352 ^b	15:46:48.400	+67:40:50.549	27840 ± 640	7.62 ± 0.11	18.04	-0.01 ± 0.01	1.60 ± 0.09
6243194942858258304 ^c	16:01:26.624	-22:44:47.033	30280 ± 900	7.37 ± 0.17	18.27	-0.16 ± 0.01	1.75 ± 0.17
4356545788311602944	16:13:30.572	-04:24:15.199	28920 ± 480	7.24 ± 0.06	17.47	-0.16 ± 0.01	1.70 ± 0.12
4450336810219872896	16:14:04.210	+07:03:18.328	17200 ± 560	7.78 ± 0.12	19.03	-0.08 ± 0.02	1.20 ± 0.26
1623581922326511104	16:23:23.508	+58:03:53.597	25300 ± 800	7.62 ± 0.14	19.04	-0.37 ± 0.02	0.90 ± 0.17
1411455519097674368	16:32:42.394	+49:36:14.602	12400 ± 220	5.54 ± 0.06	18.04	0.16 ± 0.01	0.75 ± 0.09
1426734882432542464 ^c	16:39:07.170	+54:17:47.015	12740 ± 330	7.84 ± 0.10	18.17	0.02 ± 0.02	2.88 ± 0.11
4333980859071542016	16:43:57.872	-11:52:37.772	32220 ± 1260	6.21 ± 0.25	18.28	0.06 ± 0.01	0.57 ± 0.17

Table 5 *continued*

Table 5 (*continued*)

SOURCE_ID (Gaia DR3)	R.A. (2016.0)	Decl. (2016.0)	T_{eff} (K)	$\log g$ (cm s $^{-2}$)	Gaia G (mag)	Gaia $(BP - RP)$ (mag)	Gaia Parallax (mas)
1705869136327269632	16:47:55.848	+78:02:22.207	21830 ± 670	7.74 ± 0.10	16.96	-0.20 ± 0.01	3.50 ± 0.06
1407607121025145088	16:52:48.734	+46:34:56.996	25110 ± 740	7.47 ± 0.10	18.33	-0.23 ± 0.02	1.65 ± 0.12
1408695878054997376 ^c	16:52:54.305	+48:04:05.862	14960 ± 420	7.41 ± 0.08	18.79	-0.12 ± 0.02	1.95 ± 0.15
4545581528237665024	16:56:34.296	+14:21:23.486	12760 ± 500	8.29 ± 0.09	19.34	0.22 ± 0.02	1.83 ± 0.34
1337970174853051392 ^b	17:01:25.279	+34:35:30.260	17750 ± 490	7.58 ± 0.09	18.94	-0.03 ± 0.02	1.35 ± 0.16
4568269229124267904	17:08:16.358	+22:25:51.074	21500 ± 350	6.91 ± 0.05	19.48	-0.15 ± 0.02	0.93 ± 0.26
1420761029600606592 ^{ab}	17:24:06.145	+56:20:03.073	39530 ± 4180	7.84 ± 0.35	16.26	-0.10 ± 0.01	2.48 ± 0.04
4601834943998509440	17:29:16.269	+32:08:40.438	12040 ± 590	8.09 ± 0.21	19.18	-0.11 ± 0.02	1.45 ± 0.19
1335938792758457088	17:31:56.687	+34:56:18.726	32860 ± 810	8.15 ± 0.15	18.48	-0.30 ± 0.02	1.68 ± 0.13
5921549652415561856	17:35:44.646	-54:01:52.511	21670 ± 760	4.99 ± 0.10	18.28	-0.10 ± 0.01	0.62 ± 0.17
1349206114240568960	17:37:49.760	+43:33:28.476	24040 ± 1370	7.36 ± 0.20	19.86	0.25 ± 0.04	2.01 ± 0.27
4607711764930567296	17:48:33.469	+35:03:56.747	23100 ± 920	7.88 ± 0.13	18.40	-0.03 ± 0.02	1.65 ± 0.12
4580948105722037248	17:56:10.500	+24:33:58.198	18810 ± 620	7.24 ± 0.11	17.78	-0.16 ± 0.01	2.63 ± 0.09
4580931338170148096	17:58:22.157	+24:46:45.725	21210 ± 1640	7.51 ± 0.28	19.52	-0.03 ± 0.03	1.32 ± 0.27
4583332435345090432	18:01:12.127	+27:05:19.187	26040 ± 1380	7.15 ± 0.21	15.46	-0.300 ± 0.004	6.14 ± 0.03
2122667052087422848 ^c	18:04:27.825	+48:18:39.539	18040 ± 510	7.66 ± 0.09	18.96	-0.12 ± 0.02	1.51 ± 0.15
6652309883673792256	18:08:21.306	-55:24:57.704	29940 ± 460	7.40 ± 0.05	17.65	-0.13 ± 0.01	1.78 ± 0.09
6417682795318622592 ^c	18:09:53.230	-74:43:37.769	27250 ± 1070	7.08 ± 0.17	18.33	0.02 ± 0.01	1.52 ± 0.11
2115751643640408960 ^b	18:11:43.485	+44:55:01.099	27050 ± 570	7.38 ± 0.09	17.37	-0.08 ± 0.01	2.21 ± 0.06
2123798209034064512 ^b	18:17:00.609	+50:00:50.008	32830 ± 660	7.82 ± 0.12	17.67	0.20 ± 0.01	1.60 ± 0.07
4509763077242737152 ^c	18:27:51.851	+15:16:35.663	13040 ± 430	7.95 ± 0.09	19.29	0.23 ± 0.02	1.84 ± 0.31
6650799738811684992	18:35:31.234	-54:55:55.434	24890 ± 440	7.29 ± 0.06	18.35	-0.15 ± 0.02	1.69 ± 0.17
6636129539276532608 ^c	18:36:23.992	-59:51:31.291	30610 ± 710	8.06 ± 0.14	18.09	0.09 ± 0.01	2.00 ± 0.14
2146494091832635520 ^{ab}	18:47:16.639	+53:37:49.998	34070 ± 770	7.82 ± 0.14	17.63	-0.06 ± 0.01	1.29 ± 0.07
6651387427778240128	18:49:41.321	-53:02:49.114	30890 ± 720	7.14 ± 0.13	17.94	-0.11 ± 0.02	1.13 ± 0.13
2252265701675503616	19:06:00.874	+62:39:23.713	13570 ± 210	5.34 ± 0.05	17.96	-0.06 ± 0.01	0.51 ± 0.10
6744390099848377472	19:32:54.642	-34:04:16.882	23610 ± 980	7.40 ± 0.13	17.77	-0.10 ± 0.01	2.69 ± 0.13
6645284902019884928	19:36:39.332	-52:46:00.102	30770 ± 1790	8.06 ± 0.41	17.97	-0.09 ± 0.02	1.55 ± 0.14
6864866513780069120	19:49:46.727	-21:44:11.526	20850 ± 400	7.62 ± 0.06	17.51	-0.12 ± 0.01	2.58 ± 0.10
6447432350150267392	19:53:14.631	-58:02:22.816	34200 ± 600	7.91 ± 0.09	17.05	0.21 ± 0.01	2.92 ± 0.07
6426888701236987392 ^a	19:53:37.608	-67:44:23.384	36690 ± 1730	7.72 ± 0.32	16.82	-0.06 ± 0.01	2.11 ± 0.05
6851161273137814528 ^{bc}	19:59:01.117	-25:11:43.080	32030 ± 560	7.67 ± 0.09	17.49	0.01 ± 0.01	2.35 ± 0.10
6867085976780414848 ^c	20:00:28.593	-19:30:50.785	31860 ± 3680	6.52 ± 0.73	17.96	-0.09 ± 0.01	1.51 ± 0.15
6874698381114836352 ^c	20:12:26.489	-15:03:38.736	27200 ± 520	7.42 ± 0.07	18.25	-0.12 ± 0.01	1.77 ± 0.17
6904576475726842240	20:26:41.354	-09:42:03.582	38900 ± 3530	7.51 ± 0.44	16.39	-0.19 ± 0.01	4.27 ± 0.07
1812357593394310400 ^c	20:39:43.468	+18:09:34.877	31370 ± 2450	6.22 ± 0.45	15.84	-0.290 ± 0.004	0.86 ± 0.04
6677077521256040576 ^c	20:50:18.091	-42:19:07.151	21770 ± 360	7.58 ± 0.05	17.85	-0.26 ± 0.01	1.13 ± 0.14
1757877204553173248 ^c	20:52:36.182	+12:06:43.542	33130 ± 1070	6.45 ± 0.21	16.39	-0.257 ± 0.005	0.71 ± 0.07
6805523324308751232	20:53:52.091	-25:35:15.475	24270 ± 830	7.30 ± 0.12	18.19	-0.28 ± 0.01	1.43 ± 0.19
1734921287254144640 ^c	20:56:12.309	+05:25:14.866	32410 ± 3460	5.49 ± 0.63	16.34	-0.343 ± 0.005	0.66 ± 0.06

Table 5 *continued*

Table 5 (*continued*)

SOURCE_ID (Gaia DR3)	R.A. (2016.0)	Decl. (2016.0)	T_{eff} (K)	$\log g$ (cm s $^{-2}$)	Gaia G (mag)	Gaia $(BP - RP)$ (mag)	Gaia Parallax (mas)
1764456441613885952	20:57:30.511	+16:50:14.611	22310 \pm 1250	7.71 \pm 0.19	16.56	-0.217 \pm 0.005	4.76 \pm 0.05
6479867638227626240 ^c	21:02:35.668	-48:20:01.720	21750 \pm 550	7.59 \pm 0.08	17.21	-0.19 \pm 0.01	3.08 \pm 0.09
6787236251212992896	21:08:40.254	-31:32:17.113	17270 \pm 260	7.99 \pm 0.05	17.54	-0.12 \pm 0.01	1.98 \pm 0.25
6912586070040308096 ^c	21:10:35.318	-03:58:25.378	10450 \pm 150	7.81 \pm 0.06	18.93	0.18 \pm 0.02	2.60 \pm 0.25
6579921027395679104	21:13:54.811	-43:48:22.496	19210 \pm 470	8.13 \pm 0.08	18.64	-0.25 \pm 0.02	1.63 \pm 0.21
1847044402111714944	21:27:36.602	+26:05:43.559	15040 \pm 470	7.52 \pm 0.10	19.44	0.13 \pm 0.03	1.85 \pm 0.27
1745828481256730368 ^c	21:28:23.751	+11:44:51.972	34930 \pm 3530	5.84 \pm 0.62	15.77	-0.361 \pm 0.004	0.94 \pm 0.05
6816044860312027264	21:30:07.548	-22:59:39.732	16850 \pm 560	7.64 \pm 0.11	18.66	-0.10 \pm 0.01	1.57 \pm 0.27
6828182472250027776 ^c	21:30:33.081	-22:18:02.876	34170 \pm 1290	8.01 \pm 0.29	16.30	-0.374 \pm 0.005	1.79 \pm 0.07
1797040331265541376 ^c	21:32:38.897	+22:54:47.650	33290 \pm 1970	7.13 \pm 0.42	15.67	-0.234 \pm 0.004	1.05 \pm 0.04
6814484584593326720 ^b	21:34:33.314	-25:00:05.080	32620 \pm 580	7.64 \pm 0.09	17.53	-0.03 \pm 0.01	1.62 \pm 0.11
6458294666038347520	21:34:48.160	-59:11:51.709	34950 \pm 650	7.87 \pm 0.11	18.14	-0.51 \pm 0.01	1.91 \pm 0.13
2672992211134257152 ^b	21:44:54.893	-04:09:18.277	28720 \pm 630	7.61 \pm 0.09	17.79	0.11 \pm 0.01	2.34 \pm 0.15
1769307791858602880	21:49:11.106	+15:06:37.710	21250 \pm 340	6.61 \pm 0.05	18.51	-0.18 \pm 0.02	0.68 \pm 0.18
1800183147814621056 ^c	21:51:11.472	+27:30:14.450	11900 \pm 190	5.26 \pm 0.05	17.34	0.02 \pm 0.01	0.58 \pm 0.08
1769840196004315008 ^c	21:57:15.929	+16:27:24.638	16330 \pm 470	7.91 \pm 0.08	18.63	0.07 \pm 0.02	1.85 \pm 0.21
1896689409392725504	22:01:41.417	+29:30:41.105	18680 \pm 530	7.85 \pm 0.09	18.93	0.55 \pm 0.02	1.62 \pm 0.22
1892667430216516864	22:02:04.086	+26:24:47.250	18190 \pm 430	7.33 \pm 0.07	19.12	-0.11 \pm 0.02	1.41 \pm 0.24
1776485128886007296 ^c	22:02:25.343	+18:19:43.417	32620 \pm 3360	5.12 \pm 0.60	16.30	-0.31 \pm 0.01	0.69 \pm 0.06
2614307800931271552	22:07:40.452	-10:03:19.336	12100 \pm 350	7.65 \pm 0.12	18.41	-0.07 \pm 0.02	2.02 \pm 0.26
2620773547777880832	22:09:24.045	-05:47:08.203	24640 \pm 390	7.26 \pm 0.05	18.31	-0.21 \pm 0.02	1.44 \pm 0.16
6511369569779620224	22:14:39.022	-51:47:41.935	31110 \pm 510	8.07 \pm 0.07	17.89	-0.37 \pm 0.01	2.21 \pm 0.10
6567075776645652352	22:20:02.473	-44:42:53.798	24380 \pm 540	7.53 \pm 0.08	18.56	-0.21 \pm 0.02	1.74 \pm 0.17
2703680916400302208	22:21:23.987	+02:38:36.859	21430 \pm 660	7.49 \pm 0.10	18.63	-0.19 \pm 0.04	1.42 \pm 0.24
2679330242833214848	22:21:30.821	+01:20:55.406	30150 \pm 550	7.89 \pm 0.08	16.88	-0.30 \pm 0.01	3.70 \pm 0.09
2219113776832300416 ^a	22:21:40.399	+67:14:47.364	11980 \pm 320	7.42 \pm 0.14	18.47	0.12 \pm 0.01	2.72 \pm 0.12
2626677723354947968	22:21:44.381	-04:08:59.770	16320 \pm 2310	5.79 \pm 0.39	16.38	0.24 \pm 0.01	16.51 \pm 0.07
6822591421263379200 ^c	22:22:21.437	-18:08:57.797	23380 \pm 550	7.48 \pm 0.07	18.07	-0.28 \pm 0.02	1.52 \pm 0.18
2737084320170352256	22:24:03.905	+16:04:04.030	19830 \pm 520	7.78 \pm 0.08	18.91	-0.19 \pm 0.03	1.75 \pm 0.28
1881612734154248320	22:24:46.707	+27:16:44.886	9400 \pm 160	8.39 \pm 0.19	16.54	0.37 \pm 0.01	14.57 \pm 0.10
2737737292637935232 ^a	22:29:35.774	+17:45:47.156	11780 \pm 240	8.08 \pm 0.17	16.63	-0.04 \pm 0.01	11.85 \pm 0.06
2609161983433881088	22:35:47.347	-09:09:50.645	21650 \pm 600	7.38 \pm 0.08	19.37	-0.27 \pm 0.04	1.56 \pm 0.33
2656512108086228096	22:45:08.146	+03:01:11.093	17580 \pm 440	7.69 \pm 0.08	18.90	0.24 \pm 0.03	2.53 \pm 0.29
1886328505164612864 ^c	22:57:02.142	+30:23:38.497	16600 \pm 260	6.94 \pm 0.05	18.54	0.17 \pm 0.01	2.50 \pm 0.17
2663625089324446976	23:01:09.045	+05:46:12.148	16610 \pm 380	7.75 \pm 0.07	18.95	-0.13 \pm 0.03	1.61 \pm 0.29
2411122140926644736	23:03:45.818	-14:14:47.072	39520 \pm 3620	7.68 \pm 0.39	16.96	-0.02 \pm 0.01	2.48 \pm 0.08
2663797162896215680	23:03:58.370	+06:36:08.298	13050 \pm 570	7.71 \pm 0.10	18.88	0.17 \pm 0.02	2.04 \pm 0.22
1931775516926570112 ^c	23:05:02.358	+43:02:45.524	33020 \pm 1980	6.29 \pm 0.38	16.26	-0.200 \pm 0.004	0.60 \pm 0.07
2658636742508253568 ^c	23:06:37.878	+02:24:29.606	9720 \pm 140	5.42 \pm 0.08	17.19	0.08 \pm 0.01	1.04 \pm 0.10
6378433631820188928	23:16:31.886	-75:01:46.337	28470 \pm 2360	7.75 \pm 0.45	17.71	-0.15 \pm 0.01	2.29 \pm 0.08

Table 5 *continued*

Table 5 (*continued*)

SOURCE_ID (Gaia DR3)	R.A. (2016.0)	Decl. (2016.0)	T_{eff} (K)	$\log g$ (cm s $^{-2}$)	Gaia G (mag)	Gaia $(BP - RP)$ (mag)	Gaia Parallax (mas)
2633584713667253376	23:18:56.489	-05:08:25.102	21480 \pm 340	7.82 \pm 0.05	18.47	-0.18 \pm 0.01	1.73 \pm 0.25
6501481249394275840	23:20:18.897	-51:45:36.720	15880 \pm 690	7.42 \pm 0.15	18.85	-0.17 \pm 0.02	1.99 \pm 0.19
2825856243296564608	23:22:08.733	+21:03:52.812	16680 \pm 250	6.76 \pm 0.04	19.09	0.07 \pm 0.02	0.83 \pm 0.25
2660773437198409216	23:22:30.203	+05:09:42.059	18520 \pm 330	7.18 \pm 0.05	18.75	-0.18 \pm 0.02	1.16 \pm 0.22
6528026659841832576 ^a	23:31:55.589	-47:17:56.234	24410 \pm 2320	7.40 \pm 0.33	16.89	-0.00 \pm 0.01	3.20 \pm 0.06
6523373973310305664 ^a	23:39:23.812	-48:53:50.168	30870 \pm 690	7.58 \pm 0.12	17.00	-0.33 \pm 0.01	2.20 \pm 0.06
2387618774212898944	23:46:11.487	-22:26:28.849	17220 \pm 960	7.87 \pm 0.18	19.90	0.21 \pm 0.05	1.76 \pm 0.46
2639862585760032896	23:47:32.871	-02:24:33.894	16250 \pm 270	7.05 \pm 0.05	19.03	-0.10 \pm 0.02	1.35 \pm 0.27
2867393662290131840 ^c	23:51:17.370	+29:34:35.573	22310 \pm 730	7.46 \pm 0.11	18.07	-0.21 \pm 0.01	2.18 \pm 0.14
6379389141784320640 ^c	23:57:36.404	-74:48:00.947	22440 \pm 420	7.40 \pm 0.06	18.14	-0.19 \pm 0.01	1.76 \pm 0.10
6386812017799240064 ^c	23:58:54.268	-69:56:13.639	36100 \pm 750	7.58 \pm 0.11	18.20	-0.34 \pm 0.01	1.06 \pm 0.12
2312944342501257472 ^c	23:59:12.953	-34:04:00.476	24390 \pm 520	7.87 \pm 0.07	17.81	-0.31 \pm 0.01	2.19 \pm 0.12